Graphical Abstract

Local Structure Effects on Hydrodynamics in Slender Fixed Bed Reactors: Spheres and Rings

Steffen Flaischlen, Thomas Turek, Gregor D. Wehinger

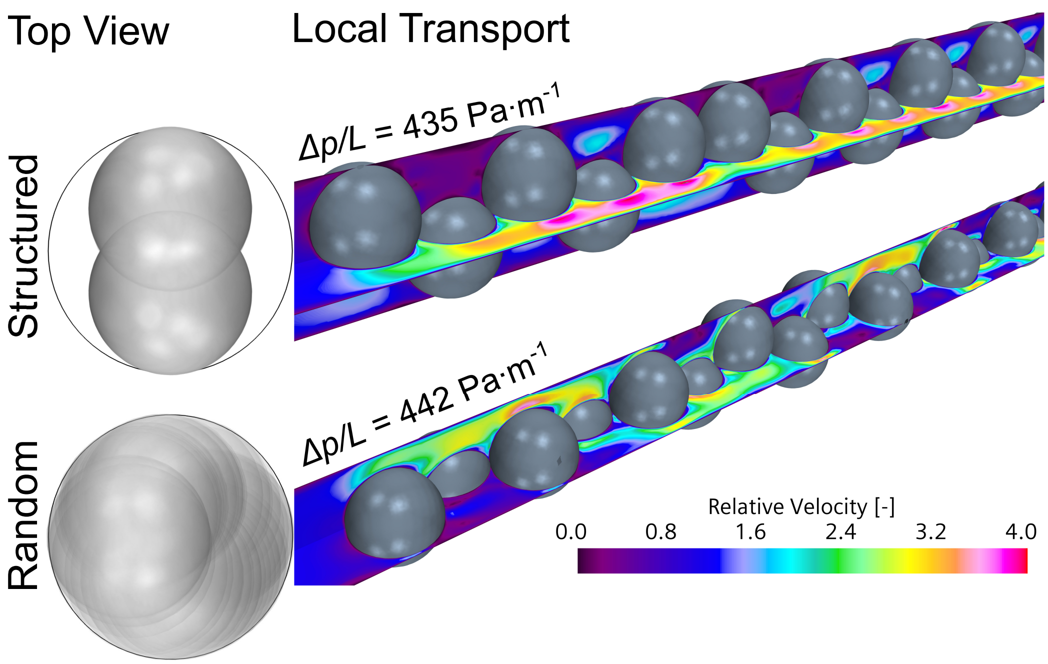

Highlights

Local Structure Effects on Hydrodynamics in Slender Fixed Bed Reactors: Spheres and Rings

Steffen Flaischlen, Thomas Turek, Gregor D. Wehinger

- Packed beds of spheres and rings are studied over wide range of $1.5 < D/d_\mathrm{p} < 9.3$
- Characterized are void fraction, tortuosity, pressure drop, residence time
- Packed bed of spheres can be clustered in four distinct regions depending on D/d_p
- Novel parameters are presented for correlations of pressure drop and tortuosity
- Excellent agreement between particle-resolved CFD and experiments

Local Structure Effects on Hydrodynamics in Slender Fixed Bed Reactors: Spheres and Rings

Steffen Flaischlen[a,b], Thomas Turek[a,b], Gregor D. Wehinger[a,b,c,*]

[a] *Institute of Chemical and Electrochemical Process Engineering, Clausthal University of Technology, Leibnizstraße 17, 38678 Clausthal-Zellerfeld, Germany*
[b] *Research Center Energy Storage Technologies (EST), Clausthal University of Technology, Am Stollen 19A, 38640 Goslar, Germany*
[c] *Institute of Chemical Process Engineering, Karlsruhe Institute of Technology, Fritz-Haber-Weg 2, 76131 Karlsruhe, Germany*

Abstract

Fixed bed reactors play a crucial role in the chemical industry, and their performance is influenced by the unique structural effects observed in the small tube-to-particle diameter ratio range ($1.5 < D/d_\mathrm{p} < 9.3$) . Experimental void fraction data for beds made of spherical and ring-shaped particles reveal sudden changes, deviating significantly from theoretical calculations. These effects, categorized into four zones for spherical particles, i.e., single particle string, central channel, annular gap, and central channel + annular gaps, exhibit varying impacts on pressure drop. To describe this, the factors of the Ergun equation are modified accordingly. Furthermore, tortuosity is introduced as an additional parameter to describe the structural effects on fixed bed behavior. Classic correlations prove inadequate, leading to the adaptation of the Millington correlation for random beds, as well as those with a central channel and/or annular gaps. With particle-resolved Computational Fluid Dynamics (PRCFD) simulations, the residence time behavior is quantified of differently structured beds of spheres and rings, revealing deviations from plug flow and the presence of stagnation zones in beds containing a central channel. Notably, beds with an annular gap displays residence time behavior akin to plug flow, with lower pressure drop and an ordered, reproducible structure. These results highlight the impor-

*Corresponding author
Email address: `wehinger@icvt.tu-clausthal.de` (Gregor D. Wehinger)

tance of the D/d_p ratio as an additional descriptor to characterize transport phenomena in slender fixed-bed reactors.

Keywords:
Fixed-bed reactor, Pressure drop, Void fraction, Tortuosity, PRCFD

---

1. Introduction

Fixed bed catalytic reactors play a crucial role in the chemical industry [1]. Due to the inherent exo- or endothermic nature of catalytic reactions, precise thermal control is imperative in the catalytic fixed bed reactors. Hence, it becomes crucial to establish and maintain a specified temperature range throughout the process. To ensure optimal heat exchange, narrow tubes arranged in tube bundles are typically used as they offer a higher heat exchange surface area relative to their volume. Additionally, the utilization of larger particles helps to minimize the pressure drop in the reactor. Consequently, fixed bed reactors with a small tube-to-particle diameter ratio ($D/d_\mathrm{p} < 10$) are preferred [2]. As a consequence of the confining wall, the fixed beds often no longer possess a random structure. Contrarily, fixed beds with a large D/d_p ratio (> 30) exhibit a random structure and tend to approach a random close pack configuration, resulting in an asymptotic value of the mean bed void fraction ($\varepsilon = Free\,Volume/Overall\,Volume$). The local void fraction, however, depends on the distance from the confining wall. Especially for low D/d_p ratios, a non-random local structure of a fixed bed leads to deviations from plug flow behavior and gives rise to a flow field with local extrema. Instead, radial profiles exhibiting local maxima and minima with a dependence on particle shape are observed [3, 4]. As the structure of the fixed bed always affects the flow, this effect is also reflected in the velocity distribution. Regions with high void fraction are associated with high velocities, and the radial velocity profile closely follows the radial void fraction profile [5, 6, 7]. The intricate structure of the fixed bed can also influence tortuosity ($\tau = actual\,pathway/direct\,pathway$), as local structural effects give rise to preferred paths within the bed. Previous studies have demonstrated the formation of highly organized structures, especially for beds of spheres with low D/d_p ratios, including annular gaps and direct channels [8, 9, 10, 11]. The fluid dynamics and heat transfer characteristics of a fixed bed are strongly influenced by its underlying structure. Traditional correlations for pressure drop and heat transfer typically rely on a single value to describe the packed bed, as well as on the plug flow assumption [12, 13]. In the Ergun equation to predict pressure drop, for instance, the fixed bed is only characterized by the void fraction value (ε), while the Eisfeld-Schnitzlein equation incorporates the wall effect through the D/d_p ratio [14, 15]. However, even the Eisfeld-Schnitzlein equation may fail to capture the specific effects within the fixed bed structure, as it assumes plug flow. Recently, Dixon [16] introduced a novel pressure drop correlation for randomly packed beds with negligible wall effects (unbounded fixed beds of spheres with $D/d_\mathrm{p} > 30$). For low D/d_p ratio beds, wall effects might influence the inertial terms. For beds with very low $D/d_\mathrm{p} < 5$ ratios, structural effects significantly influence the entire transport phenomena, which was recently shown with experimental data for radial heat transfer [10]. Describing a fixed bed solely based on spatially averaged values (void fraction, interstitial velocity, heat conductivity) may overlook the positional dependency of these effects (bed structuring and associated transport phenomena). Moreover, recent studies have shown that effects, such as the closure of a central channel, can occur with minimal changes in the D/d_p ratio, leading to the formation of a random bed structure once again [8, 10, 11]. The above mentioned studies investigated packed beds consisting mainly of spheres, and only in a relatively small range of D/d_p ratios. The overall picture of the connection between bed structure and transport phenomena is missing for slender packed beds. Currently, Particle-Resolved Computational Fluid Dynamics (PRCFD) simulations are used to model in great detail flow and associated transport in slender packed bed reactors, where the bed structure is fully resolved in three dimensions [17, 18]. Previous investigations have demonstrated the capability of PRCFD to accurately capture fixed bed structures and hydrodynamic properties, including pressure drop [19, 20] and local velocity profiles [6, 21]. Furthermore, some studies involving PRCFD have highlighted the limitations of pressure drop correlations in accounting for structural effects within fixed beds of spheres with low D/d_p ratios, see e.g. [8].

In this contribution, a broader range of tube-to-particle diameter ratios ($1.51 < D/d_\mathrm{p} < 11.5$) is considered for packed beds of spheres and hollow cylinders. These beds are studied with the combination of experiments and PRCFD simulations. The focus of this study extends beyond the analysis of the overall void fraction (with experiments and PRCFD) and encompasses a comprehensive examination of structural effects. Through the classification of these effects in the small D/d_p range, it is possible to introduce tortuosity (with PRCFD) as an additional factor for characterizing fixed beds.

Furthermore, this classification enables to elucidate the specific impact of each effect on pressure drop (with experiments and PRCFD), thus offering the opportunity to enhance existing correlations by adjusting relevant parameters. Additionally, it is assessed how these structural effects influence residence time behavior (with PRCFD), a critical parameter for the safe and efficient operation of fixed bed reactors. This understanding will facilitate the identification of optimal parameters for configuring fixed beds.

2. Methods

2.1. Experimental Setup

Tubular packed beds of spheres and hollow cylinders with various dimensions were studied experimentally in terms of void fraction determination and pressure drop measurement, see Tab. 1 for spheres and Tab. 2 for hollow cylinders. The void fraction was investigated in tubes with different diameters D, leading to a wide range of D/d_{pv} ratios, i.e., $1.51 < D/d_{\mathrm{pv}} < 11.5$ for spheres and $2.50 < D/d_{\mathrm{pv}} < 11.1$ for hollow cylinders. While d_{pv} (Eq. 1) refers to the diameter of the volume-equivalent sphere, d_{eq} (Eq. 2) refers to the equivalent diameter of a sphere with the same surface-to-volume ratio as the particle:

$$d_{\mathrm{pv}} = \left(\frac{6 \cdot V_{\mathrm{p}}}{\pi}\right)^{\frac{1}{3}} \tag{1}$$

$$d_{\mathrm{eq}} = \frac{6 \cdot V_{\mathrm{p}}}{S_{\mathrm{p}}} \tag{2}$$

Table 1: Dimensions of spheres (S) and resulting tube-to-particle diameter ratio for $D = 24.14\,\mathrm{mm}$. These particles were also packed into measuring cylinders of varying diameters for the Void Fraction investigation.

Particle label	d_{p} / mm	D/d_{p}
S1	16	1.51
S2	12.7	1.90
S3	11.5	2.10
S4	10	2.41
S5	9	2.68
S6	8	3.02
S7	7	3.45

Table 2: Dimensions of the hollow cylinders (HC) and resulting tube-to-particle diameter ratio for $D = 24.14\,\mathrm{mm}$. The particles were also filled into measuring cylinders with different diameters for the void fraction analysis.

Particle label	d_0 / mm	d_i / mm	h / mm	$d_\mathrm{i}/d_\mathrm{o}$/	D/d_pv	D/d_eq
HC1	9.5	5.5	10	0.579	2.50	4.83
HC2	9	4.8	9	0.533	2.62	4.73
HC3	8	4.6	6	0.575	3.32	6.07
HC4	6.2	4.1	5.1	0.661	4.40	9.24
HC5	4.8	2.6	4.9	0.54	4.90	8.96
HC6	2.2	1.4	2.4	0.636	11.07	23.47

The tube was filled by manually dropping one particle at a time (single particle drop) or by funnel filling for higher D/d_pv-ratios. The funnel used for this purpose had the same opening size as the diameter of the cylinder used. The void fraction was calculated by counting particles or by the weighting method with the number of particle N and the fixed bed length L:

$$\varepsilon = \frac{V_\mathrm{free}}{V_\mathrm{full}} = \frac{V_\mathrm{full} - V_\mathrm{particles}}{V_\mathrm{full}} = 1 - \frac{2 \cdot N \cdot d_\mathrm{pv}^3}{3 \cdot D^2 \cdot L} \tag{3}$$

Pressure drop was measured in an experimental setup, as described in our previous works [8, 20], with a reactor diameter of $D = 24.14\,\mathrm{mm}$ and a reactor height of 600 mm. Therefore, the pressure was determined before and after the fixed bed with two pressure sensors (Swagelok Company, Ohio, USA, model: PTI-S-AA2.5-11AQ). While the first pressure sensor was positioned directly above the fixed bed, located at the reactor inlet, the second pressure measurement was taken downstream, behind the wire mesh, which serves as the reactor's bottom where the particles are resting. The volume flow rates (2 to $60\,\mathrm{L_N\,min^{-1}}$) and working pressure (950 to 1500 mbar) were varied. The pressure drop experiments were performed 10 times for each particle type for repeatability. For each new pressure measurement, a new fixed bed was poured, resulting in a distribution of void fraction and resulting pressure drop.

2.2. Modeling and CFD Simulations

2.2.1. Synthetic Packed Bed Generation

For PRCFD simulations of packed beds, the first step is to create a sufficient representation of the fixed bed. For this purpose, a synthetic fixed bed is generated using the Rigid Body Approach (RBA). This method allows both fast simulation times for the generation of the fixed bed and an accurate representation of complex particles such as hollow cylinders [6]. The bed structures were generated synthetically with single particle drop or funnel filling with the video animation software *Blender 2.79b*, which uses the *Bullet Physics Library* for animation of rigid body collision based on Newton-Euler equations, see details elsewhere [6]. The rate at which particles were introduced into the funnel for filling in the simulation was determined by generating and releasing all particles simultaneously from various layers above the funnel. The resulting particle flow through the funnel determined the speed at which the particles entered the reactor. This approach is consistent with our experimental methodology. When the particles are at rest, the simulation is stopped and the bed structure is exported as an STL file. This is used as input for subsequent PRCFD simulations.

2.2.2. Meshing

Numerical discretization of the tubular packed beds was performed by generating a mesh consisting of polyhedral cells in the bulk and two prism cells at solid walls with the commercial CFD software Siemens Simcenter STAR-CCM+ v.15.06. The particle-particle contacts were modified using the local caps method [22, 23]. For this purpose, the particle contact zone is cut off and filled with fluid mesh cells. The cap size was kept below 1 % of the particle diameter, which is a good compromise between geometric accuracy and mesh quality, see details about meshing in packed beds elsewhere [24]. To improve the mesh quality in the small caps, the *Thin Mesher* in STAR-CCM+ was used. It provides a structured hexagonal mesh for regions, where a user-defined threshold value of the surface distance is not met. These orthogonal cells, which have angles close to 90 degrees between their edges and faces, contribute to an overall higher Cell Quality. A higher Cell Quality indicates that the cells are well-shaped and less distorted. Additionally, the use of orthogonal cells results in lower Skewness Angles, which measure the deviation of cell angles from their ideal 90-degree orientation. The meshes were generated following the guidelines based on our previous work and extended with the *Thin Mesher* method, which further enhances the quality at the particle-particle contact regions [8, 23, 25, 26].

2.2.3. CFD Model

The steady-state, isothermal CFD model is based on the conservation of mass and momentum, where the details can be found in general literature, see eg., [17]. Using the fluid density ρ and the velocity vector $\mathbf{v}$, the conservation of mass reads:

$$\nabla \cdot (\rho \mathbf{v}) = 0 \tag{4}$$

The momentum conservation reads:

$$\nabla \cdot (\rho \mathbf{v}\mathbf{v}) = \mathbf{T} \tag{5}$$

where the stress tensor $\mathbf{T}$ is described by the pressure p, the gas dynamic viscosity μ, the unit tensor $\mathbf{I}$:

$$\mathbf{T} = -\left(p + \frac{2}{3}\mu \nabla \cdot \mathbf{v}\right) \mathbf{I} + 2\mu \mathbf{D} \tag{6}$$

The deformation tensor $\mathbf{D}$ reads:

$$\mathbf{D} = \frac{1}{2}\left[\nabla \mathbf{v} + (\nabla \mathbf{v})^{\mathbf{T}}\right] \tag{7}$$

The outlet of the fixed bed simulation was set to a constant pressure of 1 atm. The gas density was calculated with the ideal gas law based on the inlet conditions of the experiments and was set to a constant value. The pressure and gas density calculation was based on the pressure measured above the fixed bed in the experiments. This pressure, along with the measured volumetric flow rate and the fluid's density, determined the inlet velocity for CFD simulations. The outlet boundary condition was set to atmospheric pressure, and due to the low pressure drop across the bed (less than 50 mbar), we assumed constant density for the calculations. All solid walls were set to the no-slip boundary condition. The pressure drop simulations were performed with STAR-CCM+ in steady-state mode, using a segregated solver with the SIMPLE algorithm for pressure-velocity coupling. In order to make a decision on the convergence of the simulation, a report was created which monitors the pressure drop of the fixed bed. The residence time simulations were performed solving the transient passive scalar transport with an implicit solver to determine the residence time distribution (RTD). Details and the formulation of the passive scalar transport equation can be found in one of our previous works [27]. The transport equation for the passive scalar component ϕ can be written as follows:

$$\frac{\partial}{\partial t}\int_V \rho \cdot \phi \cdot dV + \oint_A \rho \cdot \phi \cdot \mathbf{v} \cdot d\mathbf{a} = 0 \tag{8}$$

In this equation, the diffusion flux is neglected and thus only the convective term is considered. This was done to account only for the structural effects of the packed bed and not to obtain additional effects due to diffusion transport. This simplification aligns with the typical operating conditions in fixed-bed reactors, where low superficial velocities are rarely encountered, rendering diffusive transport negligible. Additionally, it should be noted that the objective was to provide a generalized understanding of the structural effects in packed beds, applicable across diverse processes, and thus obtain a representation independent of substance-specific diffusion coefficients. The passive scalar was set at the beginning of the bed to a value of one and the tracer concentration at the end of the fixed bed was recorded over time. The simulation time step was set to $1 \cdot 10^{-5}$ s, which guarantees a convective Courant number of less than one in all cells. The simulations were performed with five inner iterations. All simulations accounting for turbulence use the RANS (Reynolds Averaged Navier Stokes) model, where the realizable $k - \varepsilon$ turbulence model with an all y^+ wall treatment was applied. The PRCFD framework employed in this study is well-established and has been previously applied and validated against experimental data and/or correlations in multiple publications for void fraction (both mean bed and radial profiles) [6, 28], pressure drop [8, 26], heat transfer [20, 29], and chemical reactions [25, 30].

2.2.4. Derivation Tortuosity

In heterogeneous catalysis, tortuosity is typically associated with the transport of reactants and products through the pores of a catalyst particle (pore scale). However, in this study, tortuosity is employed on the pellet scale. It is utilized to characterize the intricate flow paths through the open volume of the packed bed. In this regard, it becomes a property that describes the elongation of the fluid pathway compared to a direct route through the fixed bed, thereby providing insights into the underlying bed structure. The tortuosity τ describes the enlarged pathway of a fluid passing a porous medium (see Fig. 1). In this work, the tortuosity in axial direction through the packed bed was calculated with 3D PRCFD simulations. For this, the heat and mass transfer analogy is used. Heat conduction in axial direction through the void of a packed bed of length L with adiabatic walls can be written as:

$$\dot{Q}_{\mathrm{Bed}} = -A \cdot k \cdot \frac{\varepsilon}{\tau} \frac{\Delta T}{L} \tag{9}$$

Where A is the cross sectional area of the tube, k the heat conductivity and L the length between hot and cold surface. The ratio of ε/τ is sometimes called *obstruction factor*, representing the resistance to heat conduction in comparison to a fully dense material [31]. The heat conductivity k is set to a constant arbitrary value. Between the top and bottom side of the bed, the temperature difference ΔT is set to $100\,\mathrm{K}$. The tortuosity can be calculated with the known void fraction ε, the heat flux through the bed $\dot{Q}_{\mathrm{Bed}}$ obtained from the PRCFD simulations, and the heat flux of the control volume $\dot{Q}_{\mathrm{CV}}$ with the same outer dimensions (here cross sectional area A and length L) [32, 33]:

$$\tau = \varepsilon \cdot \frac{\dot{Q}_{\mathrm{CV}}}{\dot{Q}_{\mathrm{Bed}}} \tag{10}$$

with

$$\dot{Q}_{\mathrm{CV}} = -A \cdot k \cdot \frac{\Delta T}{L} \tag{11}$$

For these simulations, only conductive heat transfer without mass and momentum transport are considered and conducted on the same computational meshes as described above.

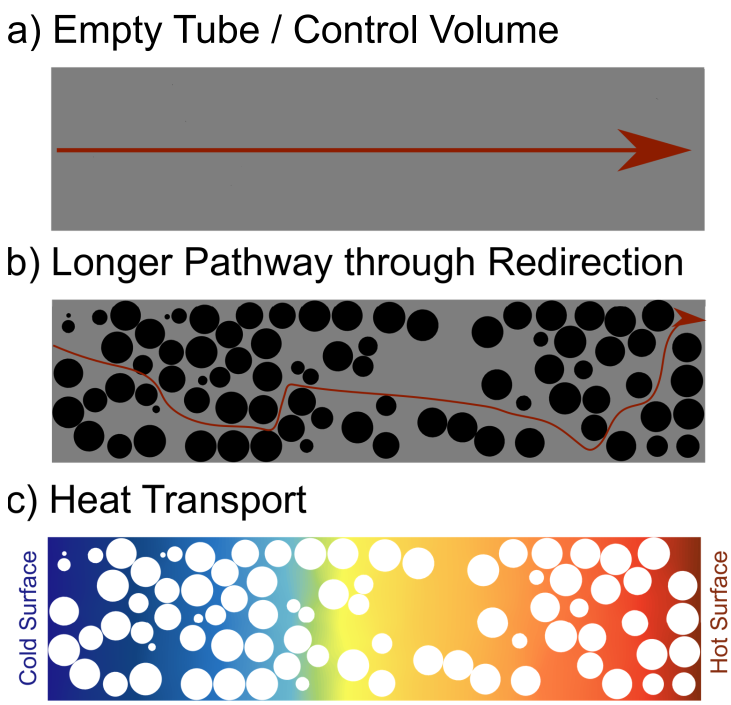

Figure 1: a) Flow through an empty pipe/control volume. b) Higher tortuosity through porous structure means longer pathways. c) Heat transport through different surface temperatures.

2.3. Literature correlations

2.3.1. Void Fraction of Packed Beds

In the case of a packed bed of monodisperse spheres, experiments have shown that void fraction is approx. 0.4, which is between that of a regular cubic arrangement ($\varepsilon = 1 - \pi/6 = 0.48$) and the densest regular spherical packing ($\varepsilon = 0.26$). In contrast, fixed beds with a small D/d_p display a higher void fraction characterized by more free space and a fluctuating pattern with respect to D/d_p [34, 35, 8]. The presence of ducts within the fixed beds contributes to this behavior, with high void fraction values indicating open ducts and low void fraction values indicating closed ducts due to particle compaction [11]. Furthermore, different random structures can exist for the same D/d_p, resulting in a void fraction distribution [36]. Additionally, the void fraction is influenced by the particle shape, uniformity of size, the filling method and particle properties, such as friction coefficients, Young's modulus, etc. [35, 8]. Due to the sensitivity of void fraction values to even minor changes in D/d_p, developing a robust correlation for description is challenging. In this study, we utilize Dixon's correlation, which exhibits a high degree of agreement with fixed beds at $D/d_\mathrm{p} < 2$, owing to its clear mathematical representation. Subsequently, it demonstrates a gradual decrease towards a value of $\varepsilon = 0.4$. It can be written for spheres as follows [37]:

$$D/d_\mathrm{p} \leq 1.865 \qquad \varepsilon = 1 - 0.667 \cdot (d_\mathrm{p}/D)^3 \cdot (2 \cdot d_\mathrm{p}/D - 1)^{-0.5} \tag{12}$$

$$1.865 \leq D/d_\mathrm{p} \leq 2 \qquad \varepsilon = 0.528 + 2.464 \cdot (d_\mathrm{p}/D - 0.5) \tag{13}$$

$$D/d_\mathrm{p} \geq 2 \qquad \varepsilon = 0.4 + 0.05 \cdot (d_\mathrm{p}/D) + 0.412 \cdot (d_\mathrm{p}/D)^2 \tag{14}$$

Dixon also gives a correlation for equilateral cylinders, which reads:

$$D/d_\mathrm{pv} \leq 1.24 \qquad \varepsilon = 1 - 0.763 \cdot (d_\mathrm{pv}/D)^2 \tag{15}$$

$$D/d_\mathrm{pv} \geq 1.24 \qquad \varepsilon = 0.36 + 0.1 \cdot (d_\mathrm{pv}/D) + 0.7 \cdot (d_\mathrm{pv}/D)^2 \tag{16}$$

For hollow cylinders, the void fraction of these fixed beds ε_hc is corrected to the basis of a full cylinder ε_fc by Eq. 17. Correcting the void fraction from hollow to full cylinders allows a comparison with Eq. 15 and Eq. 16, since a correlation for rings does not exist due to the additional degree of freedom of the inner hole.

$$(1 - \varepsilon_\mathrm{fc}) = \frac{(1 - \varepsilon_\mathrm{hc})}{a \cdot (1 - d_\mathrm{i}^2/d_\mathrm{o}^2)} \tag{17}$$

While the interpenetration of hollow cylinders can be neglected for small holes, it becomes more important for inner-to-outer diameter ratios of $d_\mathrm{i}/d_\mathrm{o} \geq 0.5$. Therefore, the factor a for considering non-penetration and interpenetration can be written as follows [37]:

$$d_\mathrm{i}/d_\mathrm{o} \leq 0.5 \qquad a = 1 \tag{18}$$

$$d_\mathrm{i}/d_\mathrm{o} \geq 0.5 \qquad a = \frac{1}{1 - d_\mathrm{i}^2/d_\mathrm{o}^2} + 2 \cdot (d_\mathrm{i}/d_\mathrm{o} - 0.5)^2 \cdot (1.145 - d_\mathrm{pv}/D) \tag{19}$$

2.3.2. Tortuosity of Packed Beds

Several different correlations were published for the determination of tortuosity in porous media, see the comprehensive review in [38]. Some of them are suitable for packed beds although the assumtions and limits might not be applied for small D/d_p-ratios, as shown in Tab. 3. All the correlations relate the mean void fraction to the tortuosity, i.e., $\tau = f(\varepsilon)$. The Bruggeman correlation [39] does not apply actually to packings of monodisperse spheres, but it is listed here since it is widely used for porous media. Furthermore, it can be seen that the correlation of Neale and Nadar [40] is by formula the same as that of Akanni [41], and thus should be valid for homogeneous random sphere packings as well as for ordered packings. It can be also seen that the correlation of Bruggeman [39] and of Millington [42] and also van Brakel [43] are only different in the exponent of the void fraction.

Table 3: Different correlations for calculation of tortuosity in porous media applicable for packed beds.

Equation	Comment	Ref.
$\tau = \varepsilon^{-1/2}$	not for monodisperse spheres	[39]
$\tau = (3-\varepsilon)/2$	ordered packings	[41, 44]
$\tau = (3-\varepsilon)/2$	random homogeneous sphere packing	[40]
$\tau = \varepsilon^{-1/3}$	homogeneous, monodisperse spheres	[42, 43]

2.3.3. Pressure Drop of Packed Beds

Pressure drop in packed beds is typically described with the Ergun equation (Eq. 20), which can be formulated by using the friciton factor f_p and the modified particle Reynolds number Re_p^* (Eq: 21)[14]:

$$f_\mathrm{p} = \frac{\Delta p \cdot d_\mathrm{eq} \cdot \varepsilon^3}{L \cdot \rho \cdot v_0^2 \cdot (1-\varepsilon)} = \frac{A}{\mathrm{Re}_\mathrm{p}^*} + B \tag{20}$$

$$\mathrm{Re}_\mathrm{p}^* = \frac{v_0 \cdot d_\mathrm{eq} \cdot \rho}{(1-\varepsilon) \cdot \mu} \tag{21}$$

where the factors A and B are the viscous and inertial terms of the Ergun equation, which are $A = 150$ and $B = 1.75$. For packed beds with confining walls and a small D/d_eq-ratio, Eisfeld and Schnitzlein [15] developed the wall correction terms A_w and B_w leading to an advanced formulation of intertial and viscous Ergun terms:

$$A = K_1 \cdot A_{\mathrm{w}}^2 \tag{22}$$

$$B = \frac{A_{\mathrm{w}}}{B_{\mathrm{w}}} \tag{23}$$

The wall correction Terms A_{w} and B_{w} are defined as follows:

$$A_{\mathrm{w}} = 1 + \frac{2}{3 \cdot (D/d_{\mathrm{eq}}) \cdot (1-\varepsilon)} \tag{24}$$

$$B_{\mathrm{w}} = (k_1 \cdot (d_{\mathrm{eq}}/D)^2 + k_2)^2 \tag{25}$$

The coefficients K_1, k_1 and k_2 are proposed for different particle shapes, as shown in Tab. 4.

Table 4: Coefficients of the Eisfeld-Schnitzlein equation Eq. (22-25) [15].

Particle shape	K_1	k_1	k_2
Spheres	154	1.54	0.87
Cylinders	190	2.00	0.77
All particles	155	1.42	0.83

Finally, Nemec and Levec developed an Ergun-type equation for the pressure drop prediction in packed beds of hollow cylinders, were the constants A and B can be written as follows, using the particle volume V and surface area S, see the original literature for more detailed formulation [45].

$$A = k_1 \cdot \left(\frac{\varepsilon^3}{(1-(1-\varepsilon)\cdot(V_{\mathrm{fc}} - m \cdot V_{\mathrm{i}})/V_{\mathrm{p}})^3} \right) \cdot \left(\frac{S_{\mathrm{fc}} + m \cdot S_{\mathrm{i}}}{V_{\mathrm{p}}} \frac{d_{\mathrm{eq}}}{6} \right) \tag{26}$$

$$B = k_2 \cdot \left(\frac{\varepsilon^3}{(1-(1-\varepsilon)\cdot(V_{\mathrm{fc}} - m \cdot V_{\mathrm{i}})/V_{\mathrm{p}})^3} \right) \cdot \left(\frac{S_{\mathrm{fc}} + m \cdot S_{\mathrm{i}}}{V_{\mathrm{p}}} \frac{d_{\mathrm{eq}}}{6} \right)^2 \tag{27}$$

The constants k_1 and k_2 were proposed by Nemec and Levec [45] with values of 150 and 1.75, identical with the original Ergun equation inertial and viscous terms. The m-value describes the fraction of the interior ring volume, which is available for fluid flow and was found by Sonntag [46] to have a value of $m = 0.2$. However, this value is based on a small database, since only four different hollow cylinders were used in that study, resulting in a scatter between $0.16 \leq m \leq 0.24$. The different ranges of validity for the shown pressure drop correlations are summarized in Tab. 5.

Table 5: Range of validity for different pressure drop correlations.

Equation	Particle shape	D/d_{eq}	$\mathrm{Re_p}$	Ref.
Ergun	Sphere	infinite	-	[14]
Eisfeld-Schnitzlein	All particles	> 1.624	0.01 to 17635	[15]
Nemec-Levec	Hollow cylinder	17.2	$\mathrm{Re}_\mathrm{p}^* < 400$	
		49.7	$\mathrm{Re}_\mathrm{p}^* < 250$	[45]

2.3.4. Residence Time Distribution in Fixed Beds

As an additional hydrodynamics characterization, the Residence Time Distribution (RTD) in packed beds of spheres and hollow cylinders is analyzed. Different flow resistances should be reflected in the RTD sum (F) and age distribution curves (E). The RTD F curve can therefore theoretically be described with Eq. 29, while Eq. 30 represents the derivative of the sum function F and thus describes the age distribution curve E depending on the dimensionless residence time θ (Eq. 28) [47]:

$$\theta = \frac{t}{\bar{t}_{\mathrm{Hy}}} = \frac{t \cdot \dot{V}}{V_{\mathrm{R}}} \tag{28}$$

Where t is the time and $\bar{t}_{\mathrm{hy}}$ is the hydrodynamic mean residence time, which can be calculated from reactor volume V_{R} and volumetric flow rate $\dot{V}$.

$$F(\theta) = \frac{1}{2}\left(1 - \mathrm{erf}\left(\sqrt{\frac{\mathrm{Bo}}{\theta}} \cdot \frac{1-\theta}{2}\right)\right) + \frac{1}{2}\left(1 - \mathrm{erf}\left(\sqrt{\frac{\mathrm{Bo}}{\theta}} \cdot \frac{1+\theta}{2}\right)\right) \cdot \exp(\mathrm{Bo}) \tag{29}$$

$$E(\theta) = \frac{\mathrm{d}F}{\mathrm{d}\theta} = \frac{\sqrt{\mathrm{Bo}} \cdot \exp\left[-\frac{\mathrm{Bo}\cdot\theta^2 + 2\cdot\mathrm{Bo}\cdot\theta + \mathrm{Bo}}{4\cdot\theta}\right]}{2 \cdot \sqrt{\pi} \cdot \theta^{\frac{3}{2}}} \tag{30}$$

Here, the Bodenstein number Bo is used, which describes the ratio between convective and diffusive transport, using the reactor length L and the axial dispersion coefficient D_{ax}:

$$\mathrm{Bo} = \frac{v_0 \cdot L}{D_{\mathrm{ax}}} \tag{31}$$

3. Results and Discussion

3.1. Void Fraction

3.1.1. Void fraction as function of tube-to-particle diameter ratio

Fig. 2 a) shows the void fraction ε as function of tube-to-particle diameter ratio D/d_{p} for spheres in blue and hollow cylinders in red. The tabulated data for the investigation of the void fraction, along with their respective standard deviations, can be found in the supplementary material. For spheres, the experiments and simulations show agreement with Dixon's correlation in the low tube-to-particle diameter ratio range. In particular, for $D/d_{\mathrm{p}} \leq 2$ there is high agreement due to the mathematical solution where only exactly one or two particles can be placed in the reactor diameter. For the range of $2 < D/d_{\mathrm{p}} = 3$, it can bee seen that the void fractions of most of the fixed beds are close to the correlation, but have still positive and negative deviations. For fixed beds with $D/d_{\mathrm{p}} > 3$ the values show a scattering behavior. Some of the fixed beds' void fractions are close to the values of a random close pack ($\varepsilon = 0.36$). Even for large ratios $D/d_{\mathrm{p}} > 10$, the asymptotic value of 0.40 is not reached. As expected, the void fraction of hollow cylinders is higher than that of spheres. In addition, the values are widely scattered and no clear trend is discernible. This might originate from the fact that D/d_{pv} is used, which does not consider the particle dimensions in detail. Therefore in Fig. 2 c), the hollow cylinder void fraction $\varepsilon_{\mathrm{hc}}$ was corrected to a full cylinder basis void fraction $\varepsilon_{\mathrm{fc}}$ with Eq. 17 and compared with the cylinder correlation of Dixon [37] (Eq. 15 and 16). In the low D/d_{pv} range, the correlation is again in reasonable agreement. Between $2 \leq D/d_{\mathrm{pv}} \leq 3$, the void fraction of the particles HC2, HC3, HC4, and HC5 varies very strongly, while in the range of $5 \leq D/d_{\mathrm{pv}} \leq 7$ the particles HC2, HC3, and HC4 have similar void fraction values.

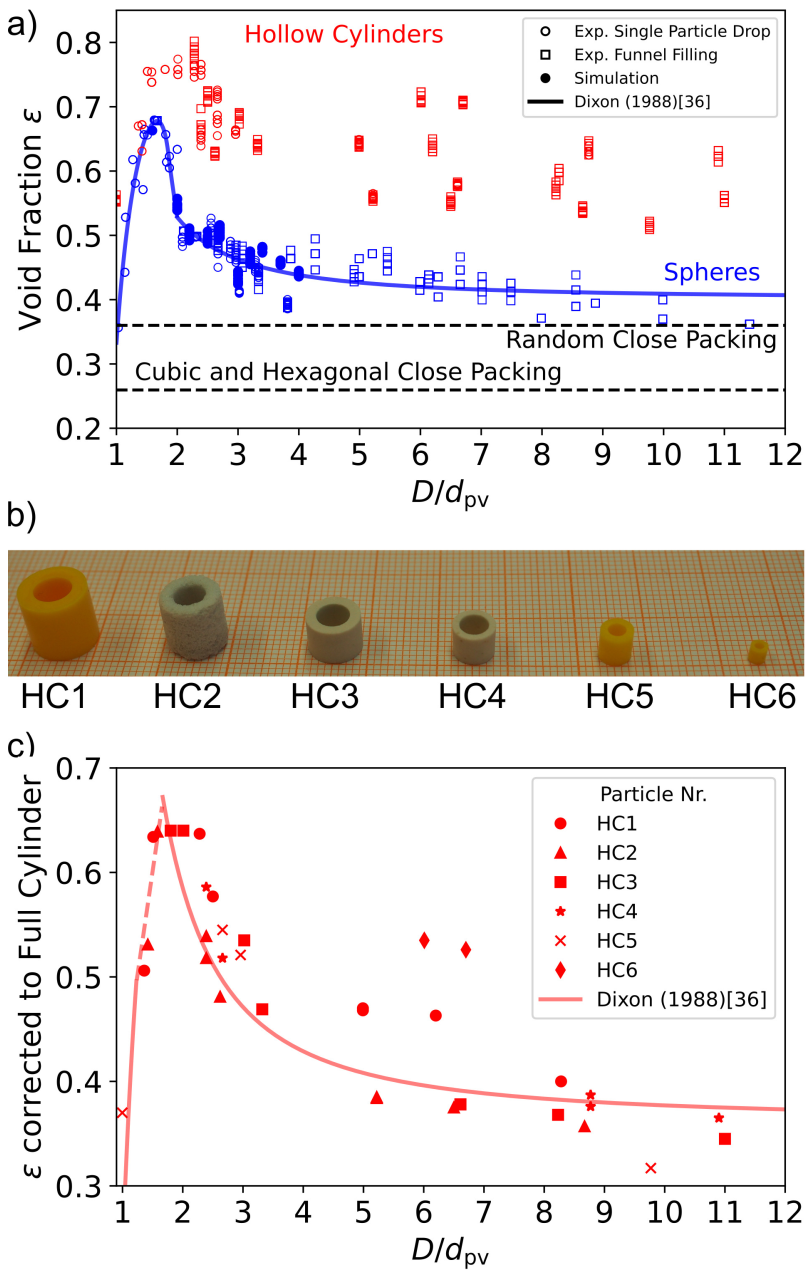

Figure 2: a) Void fraction of slender fixed beds made of spheres (blue) and hollow cylinders (red) depending on the D/d_{pv}. b) Different hollow cylinders used for void fraction experiments c) Mean void fraction of hollow cylinders $\varepsilon_{\mathrm{hc}}$ from Fig. 2 a) corrected to void fraction of full cylinders $\varepsilon_{\mathrm{fc}}$.

Large changes in bed void fraction can also result from the degrees of freedom of hollow cylinders. While a sphere has only one degree of freedom, the ring has three (outer diameter d_o, inner diameter d_i, and particle height h). One influencing factor can be the aspect ratio of the particles, since an alignment with an aspect ratio not equal to one leads to different heights of a particle layer and thus of the fixed bed. In addition, the orientation affects how many particles per layer fit into a fixed bed. While an upright cylinder can better conform to the round outer wall, allowing more particles to fit into the outermost layer, this is not possible with a horizontal cylinder, see [6]. While this explanation remains valid for the lower D/d_pv range, the influence of this wall effect diminishes as D/d_pv values increase. The noticeable fluctuations in behavior and deviations from the correlation within this range can be attributed to the inherent particle geometry. The d_pv parameter, despite its utility, offers a limited representation, as it fails to consider the nuanced interplay of the hollow cylinder's outer and inner diameters, as well as its height. These factors collectively exert influence on the bed structure and can lead to disparate void fraction values even when d_pv values appear similar. For different data points with the same D/d_pv ratio, two filling methods (single particle drop and funnel filling) were used. As noted, single particle filling is a method that results in more densely packed beds, as funnel filling can form stable particle arches due to the rapid filling. These stable bridges protect the underlying area from being filled with particles. Moreover, this influence of the filling method appears to play only a minor role at larger D/d_pv ratios.

3.1.2. Radial Void Fraction

Fig. 3 shows the radial void fractions and the transmitted light image of selected synthetically generated packed beds, which allows a view from the top of the bed to the bottom, using low opacity for the particles [20]. Thus, regions of high (dark) and low (bright) particle mass are visible. The void fraction of the spheres in Fig. 3 a) shows a region of high void fraction in the center of the fixed bed. This region can be described as a *Central Channel*, which extends almost continuously over the entire fixed bed, as already described in Flaischlen et al. [8]. In contrast, this region is nearly closed for the bed with $D/d_\mathrm{p} = 2.7$. The void fraction in the center also increases, but it is not as high as for $D/d_\mathrm{p} = 2.68$. It can also be seen, that the void fraction in the fixed bed center decreases due to the particles blocking the channel.

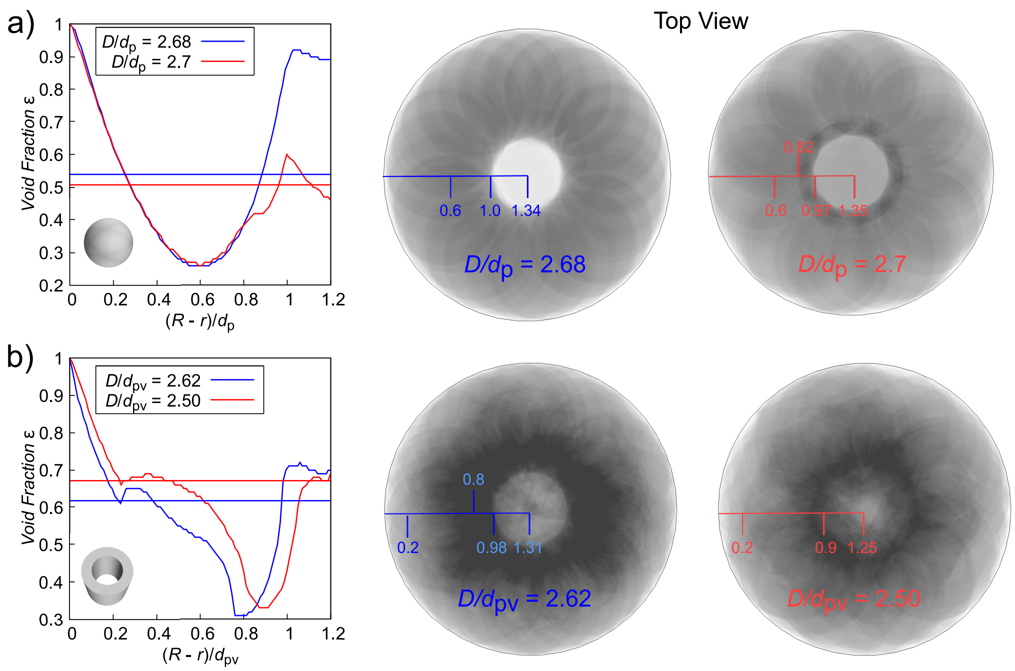

Figure 3: Radial void fraction and transmitted light image of the fixed bed for a) spheres and b) hollow cylinders. The numbers in the right pictures indicate the radial position of minima and maxima of the void fraction profiles.

In Fig.3 b), the radial void fractions of two hollow cylinder beds with nearly the same D/d_{pv} are shown. While the overall view of the radial void fraction appears to be very similar for both beds, there is a difference toward the center (Fig. 3 b). The bed with $D/d_{\mathrm{pv}} = 2.62$ (blue line) reaches a large plateau of the void fraction after $(R - r)/d_{\mathrm{pv}} = 1$, meaning one particle diameter (d_{pv}). For the bed with $D/d_{\mathrm{pv}} = 2.50$ (red line), there is only a small plateau, but not as pronounced as for the other bed. Before reaching this plateau, there is an extended sink in the void fraction. This can also be seen in the transmitted light image of all particles (Fig. 3 b)). The particles in this zone between $0.8 < (R-r)/d_{\mathrm{pv}} < 1$ leads to a more pronounced open channel in the center of the fixed bed. These examples show how an only small change of the tube-to-particle diameter ratio can drastically influence and finally change the local bed structure.

3.2. Tortuosity

3.2.1. Spheres

The influence of tortuosity can be examined illustratively with a fixed bed with $D/d_\mathrm{p} = 1.51$, see the graphical abstract for a visualization. Since the reactor to particle diameter ratio is less than two, only one particle can be placed in the cross section of the tube. This leads to packed beds that have the same void fraction in each case. Nevertheless, the fixed bed structure can be different, resulting from a change of the particle position on the cross section. An extreme case of this packed bed, where the centroids of the particles coincide to two positions, leads to the formation of a channel to the left and right of the particles. This is in contrast to a bed, where all particles are in a random structure and no channel occurs. To create the model of the structured fixed bed, we employed an animation technique integrated into Blender's Rigid Body method. We defined two planes as boundaries and used them as walls, manipulating their positions to push the particles into place. This process resulted in the creation of the structured configuration with the two lateral channels. These channels in the structured bed leads to lower flow resistance and higher velocities compared to the disordered bed. While the void fractions of the beds remain the same, the pressure drop of the two beds is different due to the different flow resistances. Since pressure drop correlations only depend on the void fraction, they cannot describe these differences. In fact, the structured bed has a lower fixed bed tortuosity due to the direct channel, see Tab6.

Table 6: Tortuosity and pressure drop at $\mathrm{Re_p} = 2300$ of two different bed structures with $D/d_\mathrm{p} = 1.51$.

	Void Fraction	Tortuosity	$\Delta p/L$ / $\mathrm{Pa\,m^{-1}}$	
			CFD	Ergun
Structured	0.663	1.234	435	525
Random	0.663	1.249	442	525

In Fig. 4 the tortuosity as a function of the D/d_pv ratio is shown for packed beds of spheres derived from synthetically generated beds and correlations. The fluctuating course can be described with the fluctuations in the void fraction, but also with the structural effects of the fixed beds. It is also noticeable that no correlation can reproduce the derived tortuosities from the synthetically generated packings. The Bruggemann correlation gives the highest τ values, whereas the Millington correlation gives the lowest values. The deviations can be explained with the different assumptions of the correlations. While the Bruggeman correlation is restricted to non-monodisperse particle packings, the Millington equation was originally developed for steady diffusive flow through porous solids. The generally expected behavior is that the void fraction with increasing D/d_{pv} can drop to a minimum limit value (Fig. 2), which is then also directly reflected in the tortuosity, which thus strives towards a maximum limiting value (Fig. 4).

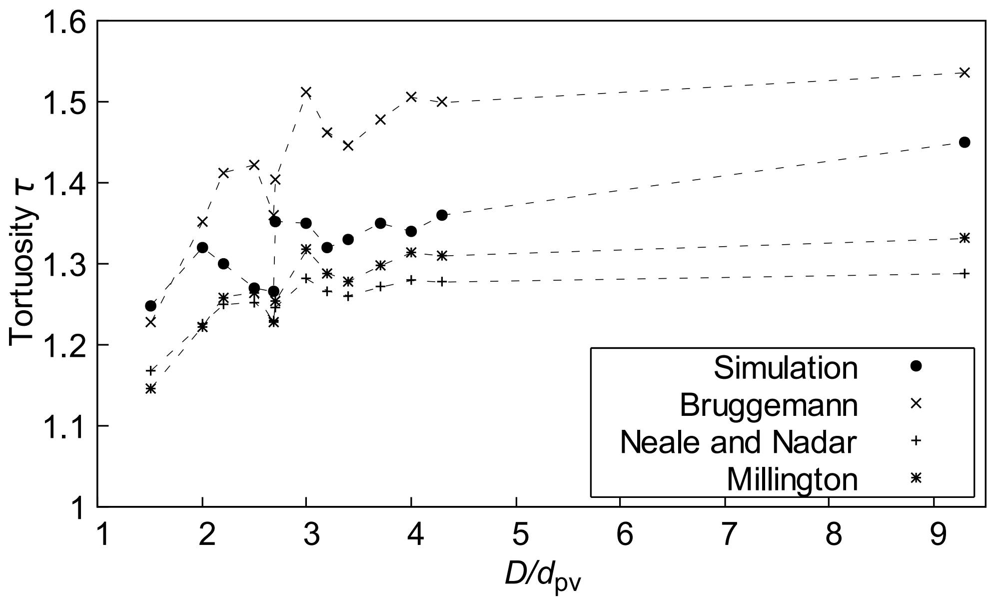

Figure 4: Tortuosity τ of the fixed beds of spheres as a function of D/d_{pv} ratio. Correlations calculated with void fraction ε obtained from simulations.

The reasons for the fluctuating behavior of tortuosity (and void fraction) can be explained by the structure of the fixed bed, i.e., the wall or central channel and an annular channel between the wall-nearest particles and the bulk. To illustrate these effects, transmitted light images are shown for all synthetically generated fixed beds from Fig. 4, in which zones of high and low particle density can be identified, see Fig. 5. Although these transmitted light images were not validated, they provide valuable qualitative insights into the three-dimensional packing structure. In these images, one can easily follow the formation of the structural effects and thus explain the behavior of tortuosity. For $D/d_\mathrm{p} = 1.51$, only one sphere fits into the cross section of the reactor. The formation of a regular structure is unlikely here, instead a random bed is formed. The center of the reactor is always filled with particles (dark gray zone) while the near-wall zones contain a smaller particle mass due to the displacement of the particles (light gray zones). These bed structures can be called single pellet string.

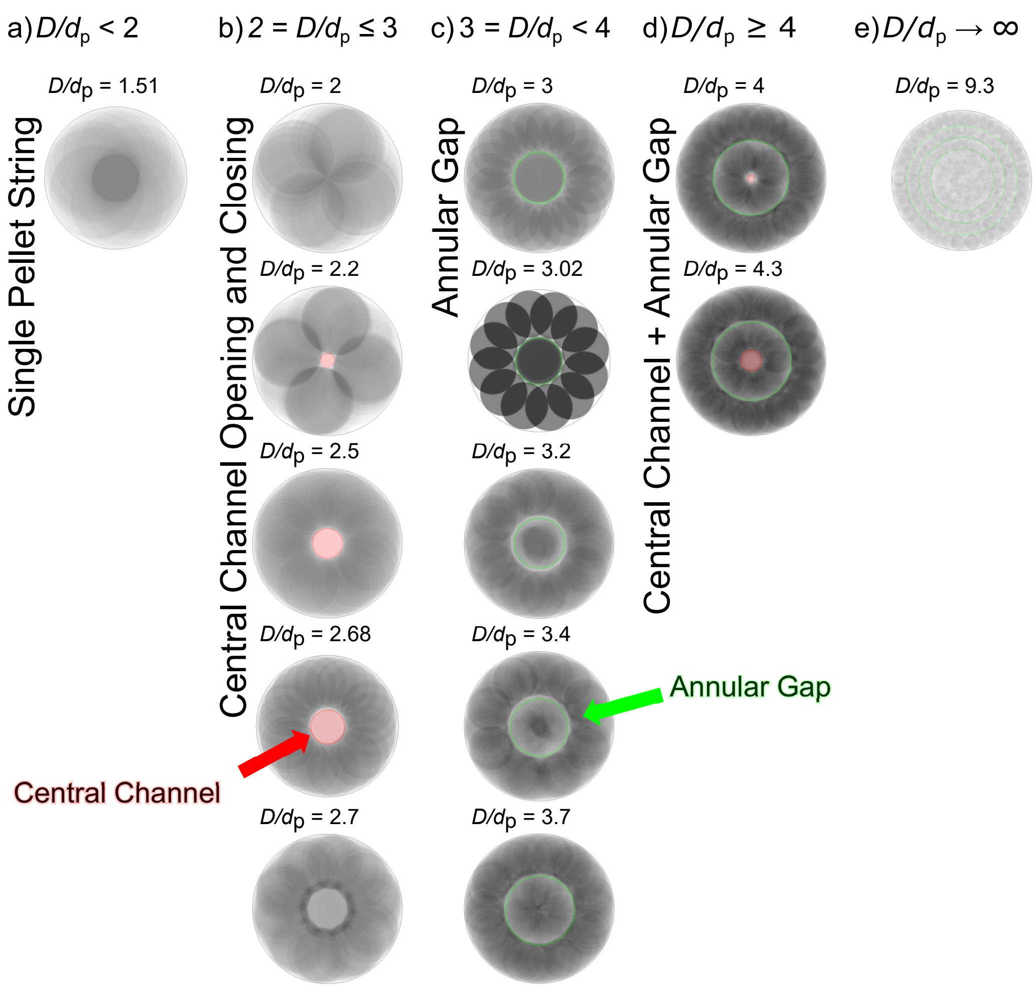

Figure 5: *Transmitted Light Image* of the synthetic fixed beds with the occurring structural effects highlighted in red (*Central Channel*) and green (*Annular Gap*).

For $D/d_\mathrm{p} = 2$, the developing structure in the fixed bed results in an almost uniform distribution of particles over the reactor cross section. The pressure drop of this bed can also be reproduced with correlations, see [8], so that this bed has no special structure effect. If D/d_p increases, this leads to an opening in the center of the reactor. This channel (marked red in Fig. 5) opens and becomes larger with increasing D/d_p. In this region, the pressure drop of the fixed beds cannot be calculated with existing pressure drop correlations. Moreover, the effect of the channel can be seen in the tortuosity in Fig. 4, as it becomes lower starting from the value of $D/d_\mathrm{p} = 2$. At $D/d_\mathrm{p} = 2.7$, the closure of the channel occurs. This behavior is characterized by a sudden increase of tortuosity. For this fixed bed, the pressure drop can again be reproduced by a correlation, as shown in [8], which is why it can again be assumed that there are no structural effects. Further increase of $D/d_\mathrm{p} > 3$ results in a small decrease of the tortuosity (which is against the general trend of an increase up to a maximum limit). This behavior can be explained by the *Annular Gap* (in green) that forms around spheres located in the center. Interesting to notice is the fixed bed structure for $D/d_\mathrm{p} = 3.02$, which is highly ordered. In addition to the *Annular Gap* in this very special configuration, the structure is highly ordered, no particle is in a random position. This leads to very distinct wall channels, which appear as completely white areas in the *Transmitted Light Image*. The *Annular Gap* first becomes larger (decreasing tortuosity until $D/d_\mathrm{p} = 3.2$ and is then partially blocked by particles, but not completely closed (slightly increasing tortuosity). At $D/d_\mathrm{p} = 4.0$ the tortuosity decreases again, because at this point the following two effects combine. An *Annular Gap* is formed around the inner particles, as well as a channel in the center of the reactor. In the following, the tortuosity increases slightly again, since the channel and the *Annular Gap* are blocked by particles. Nevertheless, due to the structural effects, the tortuosity increases only slightly to the level already reached at $D/d_\mathrm{p} = 3.0$. In addition, a bed with $D/d_\mathrm{p} = 9.3$ (Fig. 5 e)) is shown, where regular *Annular Gaps* can be identified. They can be found in the wall near area, with an decreasing structure to the center of the bed. In the bed center, the structure becomes random, so that *Annular Gaps* are no longer found. This results in the typical oscillating pattern of the radial void fraction with distance from the wall, described e.g. by the equation of De Klerk [48]. The overall appearance of the *Transmitted Light Image* is also a very uniform gray scale, indicating that the structure of the *Annular Gap* is not very pronounced and thus plays a minor role in the flow properties of the bed. In this range, the pressure drop can again be predicted with an appropriate correlation. Investigations on larger D/d_pv ratios were not performed, but it can be assumed that from this point on the local structure plays a minor role.

In agreement with the results of Dixon [10], the fixed beds can be classified into categories depending on the ratio of D/d_p. In the *Single Pellet String* class, no local structure could be observed, see Fig. 5 a). While the centered channel occurs in the range $2 = D/d_\mathrm{p} \leq 3$, this category was referred by Dixon to as the *Highly Structured Range* class. Because of the visible effect, where the particles arrange on the outer wall until the channel is closed by a centered particle (see Fig. 5 b)) we would classify this as *Central Channel*. In the third class, the particles are only "weakly structured" Dixon [10]. An *Annular Gap* around the centered particle occur, see Fig. 5 c), which can be referred to as the *Annular Gap*. While for $D/d_\mathrm{p} \geq 4.0$ the fixed bed tends to become unstructured (cf. Dixon 2021 [10]), local effects are still visible in the *Transmitted Light Image* (Fig. 5 d)). This class combines the effects of the last two classes and could be named *Central Channel + Annular Gap*.

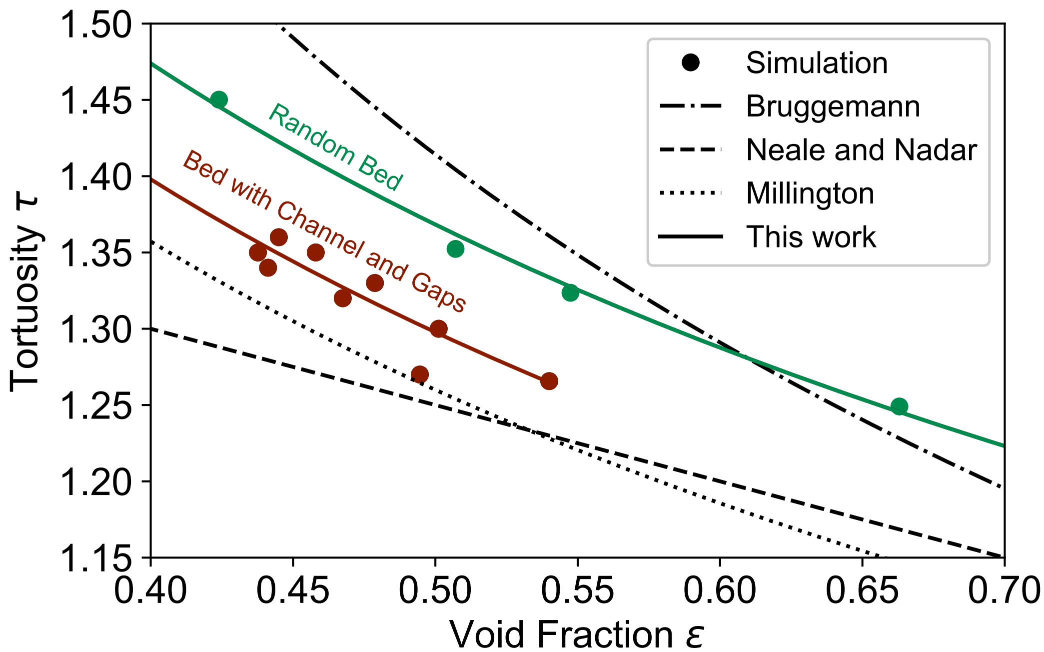

Figure 6: Tortuosity τ as a function of void fraction ε for packed beds of spheres.

In Fig. 6, tortuosity is considered as a function of void fraction showing the values obtained from the synthetically generated beds and the correlations from Tab. 3. The results of the synthetically generated beds can be divided into two categories: beds with *Central Channel* and/or *Annular Gaps* (red) and random bed structures (green in Fig. 6). The random packed beds are $D/d_\mathrm{p} = [1.51; 2.0; 2.7; 9.3]$, and if only these are considered, a clear trend can be seen and described ($R^2 = 0.99$) with the following formula:

$$\tau = 1.086 \cdot \varepsilon^{-1/3} \tag{32}$$

The form of the obtained correlation is identical to the Millington equation $\tau = \varepsilon^{(-1/3)}$ [42]. The difference here is only the shift due to the newly introduced prefactor. Similarly, the tortuosity of the fixed beds with channel and/or gaps can be described by Eq. (33), although a larger scattering of values can be observed here ($R^2 = 0.81$).

$$\tau = 1.03 \cdot \varepsilon^{-1/3} \tag{33}$$

This equation is valid for the investigated random fixed beds with:

- *Central Channel*: $2 < D/d_\mathrm{p} < 2.7$
- *Annular Gap*: $3 \leq D/d_\mathrm{p} < 4$
- *Central Channel + Annular Gap*: $4 \leq D/d_\mathrm{p} \leq 4.3$

In contrast to Eq. (32), however, Eq. (33) is valid only up to a value of $\varepsilon = 0.55$. This validity results from the minimum D/d_p ratio. In Fig. 2 it can be seen that fixed beds exceeding this void fraction ε are exclusively in the range $D/d_\mathrm{p} < 2$, in which in reality random structures occur.

3.2.2. Hollow Cylinders

Subsequently, the tortuosity of the hollow cylinder fixed beds are compared. The tortuosity was calculated only for the hollow cylinder fixed beds, which were studied experimentally in terms of pressure drop, see. Tab. 7.

Table 7: Tortuosity of packed beds of hollow cylinder.

D/d_pv	τ
2.50	1.305
2.62	1.299
3.32	1.449

While between $D/d_{\mathrm{pv}} = 2.50$ and $D/d_{\mathrm{pv}} = 3.32$ an increasing trend of tortuosity can be seen, it remains approximately the same for $D/d_{\mathrm{pv}} = 2.62$. This indicates a local structure effect occurring in this fixed bed configuration. Therefore, the pressure drop of the packed beds will be compared, since it has already been shown that local structural effects have a measurable influence on it.

3.3. Pressure Drop

The local structure has an influence on the flow properties. This can be shown with the pressure drop as a representative value. In the following, the pressure drop of different shaped particles is investigated in terms of the local structure effects.

3.3.1. Spheres

It was already shown in Fig. 5 that the local structure can be divided into different categories. In the next step, the pressure drop is represented as the dimensionless friction factor f_{p} versus the modified particle Reynolds number $\mathrm{Re_p}^*$ (Eq. 20). In Fig. 7 the values are compared with the pressure drop correlation of Ergun (black), which is using the factors $A = 150$ and $B = 1.75$ and an area of $\pm 20\%$ (grey). While the random fixed beds ($D/d_{\mathrm{p}} = [1.51; 2.0; 2.7; 9.3]$) are within this range, the deviation becomes larger for the beds with a *Central Channel* or *Annular Gaps*. Because of the clearly visible trend of the different effects, the Ergun coefficients are adjusted for them. In Fig. 7 the Ergun equation is shown with modified inertial and viscous resistances A and B.

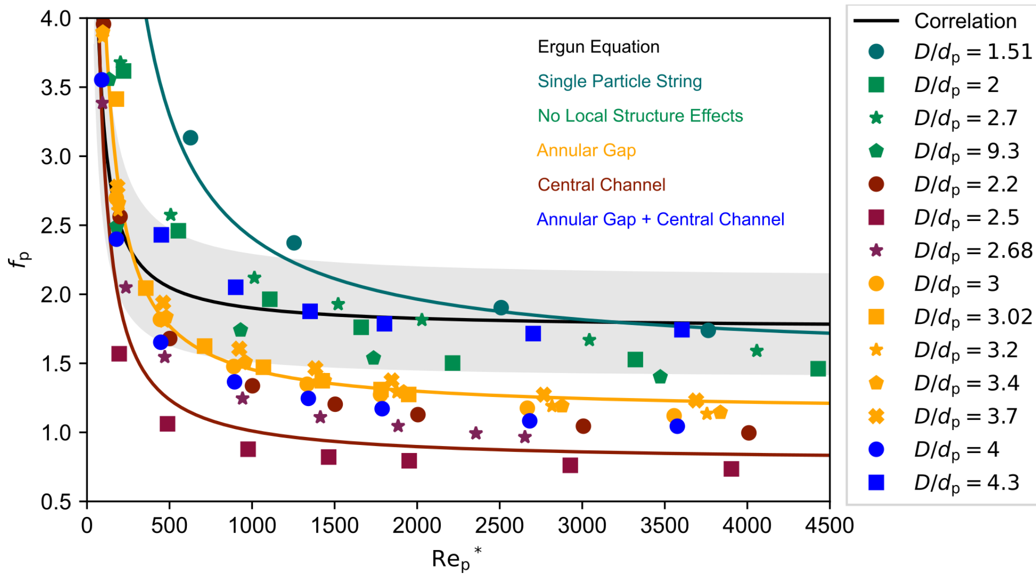

Figure 7: Friciton factor over Re_p^* in fixed beds of spheres without and with local structure.

It is clear visible that the Ergun equation overestimates the pressure drop, and also that the different local structure categories have a different influence on the pressure drop behavior. The *Single Particle String* with $D/d_\mathrm{p} = 1.51$ shows agreement with the Ergun Equation in the range of higher particle Reynolds numbers ($\mathrm{Re}_\mathrm{p}^* > 1500$) while in the lower range, the friction factor is overestimated. This can also be seen in the fitted viscous (A) and inertial (B) terms (Tab. 8), representing the linear and quadratic depending of pressure drop Δp on superficial velocity v_0. While the linear Term A is way higher than the original Ergun value, the quadratic term is only 15 % smaller, leading to a reasonable agreement for $\mathrm{Re}_\mathrm{p}^* > 1500$. The *Central Channel* lowers the pressure drop with the highest values, but also with a high scattering around the fitted Ergun parameters ($R^2 = 0.73$). Reason for this behavior is the different flow resistance, resulting from the channel width. While the *Central Channel* begins to open for $D/d_\mathrm{p} = 2.2$, it reaches the maximum in this work shown width at $D/d_\mathrm{p} = 2.5$. At this ratio, the channel is completely open over the entire fixed bed. At $D/d_\mathrm{p} = 2.68$, the channel is also open, but starts to become partially blocked, leading to an increase in the pressure drop. In contrast, it can be seen that the *Annular Gap* has the lowest effect on pressure drop, for different D/d_p ratios. Nevertheless, the *Annular Gap* also leads to a deviation of more than 20%

compared to the original Ergun equation. Here, the Ergun parameters can be fitted with a coefficient of restitution of $R^2 = 0.97$, showing that the different *Annular Gap* widths have almost the same effect on the pressure drop. The combination of the two effects (*Annular Gap + Central Channel*) leads for $D/d_\mathrm{p} = 4$ to a pressure drop between the two individual effects resulting from the small *Central Channel* which could be identified as the major effect on pressure drop. An increase of D/d_p now leads to an agreement with the original Ergun parameters, resulting from the partially blocking of *Central Channel* and *Annular Gap*.

Table 8: Modified porous inertial (A) and viscous (B) resistance factors.

Structure Effect	D/d_p	Re_p^*	A	B	R^2
No	infinite	-	150	1.75	-
Single Particle String	1.51	> 250	889	1.52	0.99
Annular Gap	$3 \leq D/d_\mathrm{p} < 4$	≥ 200	315	1.14	0.97
Central Channel	$2 \leq D/d_\mathrm{p} < 2.7$	≥ 200	252	0.87	0.73

3.3.2. Hollow Cylinders

Classical pressure drop correlations, such as the Ergun [14] or Eisfeld-Schnitzlein [15] equations, can underestimate the pressure drop compared to measured results because of the high void fraction resulting from the hollow cylinder inner hole volume. However, not all of the interior of the hollow cylinder is available for flow, resulting in a smaller actual cross-sectional area. While the correlations are fitted for a large number of different particles, it is possible that the hollow cylinders may be given an orientation that allows higher flow through the internal volumes. Therefore, specialized correlations have been developed for predicting the pressure drop in beds of hollow cylinder. One of these is the Nemec-Levec equation (Eq. (26-27)), in which the cross-sectional area is reduced by the m-value that describes the flow through the ring inner volume. This can be seen in the cut scenes through the beds, shown in Fig. 8, where the velocity inside the inner volume is very low.

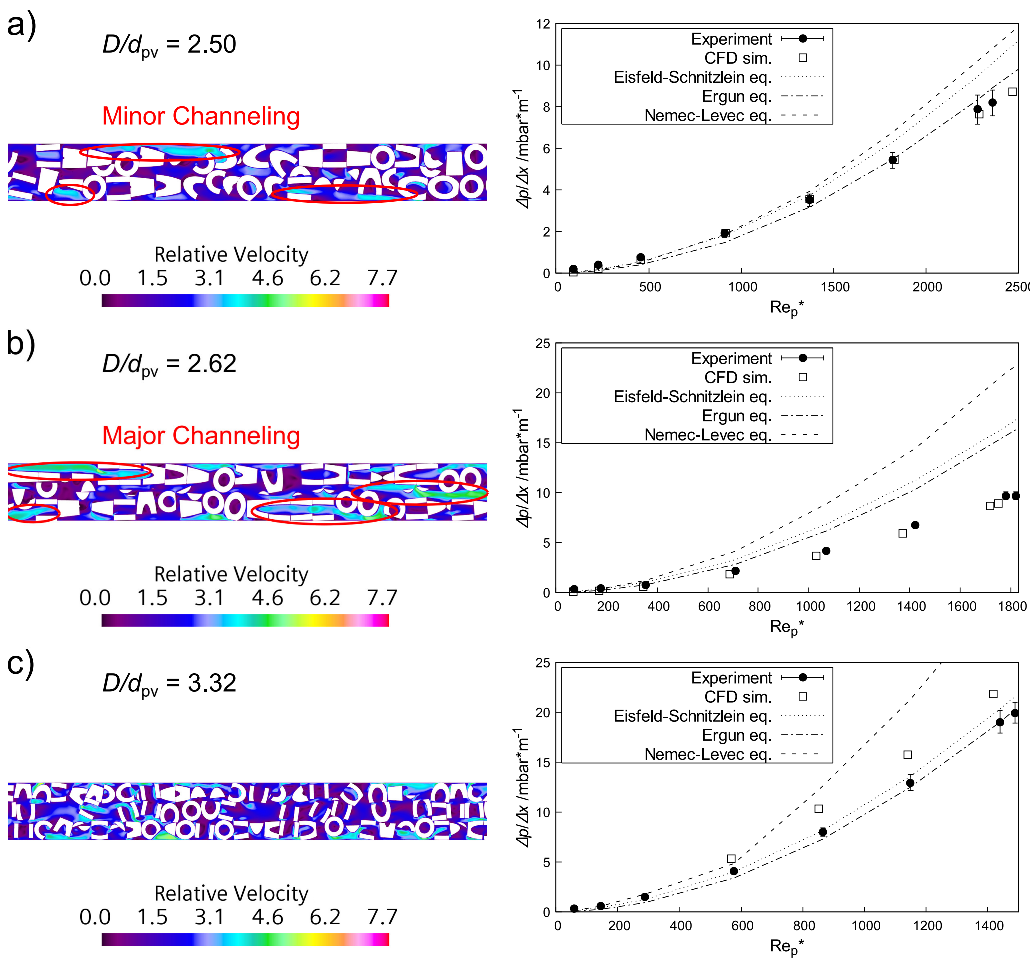

Figure 8: Pressure drop as a function of Re_p^* in fixed beds of hollow cylinders for different D/d_pv. Velocity scenes through the bed and comparison of pressure drop correlations with the CFD simulations.

The first bed with $D/d_\mathrm{pv} = 2.50$ can be reproduced very well with CFD simulations. Also the standard pressure drop correlations of Ergun (Eq. (20)) and Eisfeld-Schnitzlein (Eq. (22 - 25)) show agreement with the experimental results, especially in the low Re_p^* range. The specialized correlation of Nemec-Levec (Eq. (26-27)) also shows agreement for low Re_p^*, but deviations occur for flow exceeding $\mathrm{Re}_\mathrm{p}^* = 1500$. It should be mentioned that the values used for development of the Nemec-Levec equation are in a lower Re_p^* range (see Tab. 5). In the PRCFD, it can be seen that due to the small D/d_pv ratio of this bed, some smaller channels form between the particles and the wall. Compared to the *Central Channel* which can form in fixed beds of spheres, here, no channel is formed along the entire length of the bed. The second bed studied has only slightly smaller particles with $D/d_{\mathrm{pv}} = 2.62$. While the particles are getting smaller, an increase in pressure drop is expected. Instead, the experimental values are in the same range as for the bed before. Nevertheless, the structure changes a lot, larger channels are now formed, resulting from stacked particles and a reduction of flow resistance. This leads to a strong overprediction of the pressure drop by the correlations, while the PRCFD simulations again agree with the experimental results. Also, the Nemec-Levec equation shows the highest deviation, while Ergun and Eisfeld-Schnitzlein equations predict similar but higher values. It turns out that the behavior of tortuosity found in Tab. 7, indicating a structural effect, is reflected by the pressure drop, since it cannot be well reproduced by the typical correlations. The third bed consists of hollow cylinders forming a D/d_{pv} ratio of 3.32. Compared to the second bed, the stacking of particles is not as pronounced. Additionally, at this d_{pv} ratio, the wall channel is not as pronounced as for $d_{\mathrm{pv}} = 2.50$. Thus, no channel formation is observed, and the flow velocity in radial and axial directions remains homogeneously distributed. The PRCFD results for this bed are slightly higher than observed in the experiments but are also within an acceptable range. Explanation for this behavior can be found in the alignment of the particles, which also can be slightly different between different experiments as well as between the PRCFD simulations. While the Ergun and Eisfeld-Schnitzlein equations again agree with the data, the Nemec-Levec equation tends to overestimations. We also utilized data fitting techniques to fit the Nemec-Levec equation in an effort to capture the intricate behavior of rings. Nevertheless, the outcomes revealed notable dispersion in the derived factors. This dispersion underscores that the derived factors are only suitable for their respective geometries, highlighting the lack of universally applicable correlations. Details are presented in the Supporting Information. Table 9 summarizes the average percentage and absolute deviations between the pressure drop of the experiments and CFD as well as correlations for the different hollow cylinder particles fixed beds. It should be noted that the deviations of the CFD simulations, approx. 20 %, originates mainly from the deviations in the smaller Re_{p} range. However, it should be noted that the error of the pressure gauges in this range is also larger. Nevertheless, it can be seen that the CFD results show a smaller deviation than the correlations.

Table 9: Mean absolute and relative deviations of pressure drop from experimental data.

D/d_{pv}	CFD		Ergun		Eisfeld-Schnitzlein		Nemec-Levec	
	$\mathrm{mbar\,m^{-1}}$	%	$\mathrm{mbar\,m^{-1}}$	%	$\mathrm{mbar\,m^{-1}}$	%	$\mathrm{mbar\,m^{-1}}$	%
2.50	0.12	18.36	0.36	32.36	0.66	29.14	0.93	34.77
2.62	0.28	21.46	2.41	49.4	2.91	56.18	5.04	89.19
3.32	2.94	25.77	0.44	26.52	0.56	17.06	5.12	44.43

3.4. Velocity Components

The results have shown that the use of correlations does not provide a reliable prediction of the pressure drop for all fixed bed structures. Due to structure effects, overestimation of pressure drop, and thus a different flow behavior may occur. Since in fixed bed of spheres the reason for the failure of the correlation was relatively easy to identify qualitatively (forming of strong structural effects see Fig. 5), it becomes more difficult for more complicated particle shapes, such as hollow cylinders, where few stacked particles lead to lower flow resistance (see Fig. 8). In the following, beds with nearly the same D/d_{pv} ratio but different local structures are compared in terms of velocity components.

The profiles for the axial, radial, and tangential velocity components as a function of the radial coordinate $(R-r)/d_{pv}$ from the PRCFD simulations are shown in Fig. 9. For the bed of spheres with $D/d_p = 2.68$, the channel is clearly visible as the axial velocity increases toward the center of the fixed bed (Fig.9 a). At the same time, for the fixed bed of spheres with $D/d_p = 2.7$, the axial velocity remains low in the center, while it is higher at the reactor wall. It can also be seen that the mean value of the axial velocity is almost the same for both beds. Fig.9 b) and c) show the radial and tangential velocity components, respectively, for the beds of spheres. The higher these components, the larger lateral mixing. While the general velocity profile appears to be very similar, the radial velocity for the fixed bed without a *Central Channel* ($D/d_p = 2.7$) is significantly higher. In summary, the two beds do not show much difference in the average axial velocity (horizontal line), but are very different in tangential and radial velocities (approx. 25 %). These much higher velocities in the non-axial direction result in longer flow paths through the bed, intensified lateral mixing, and thus a higher pressure drop than in the bed with a central channel.

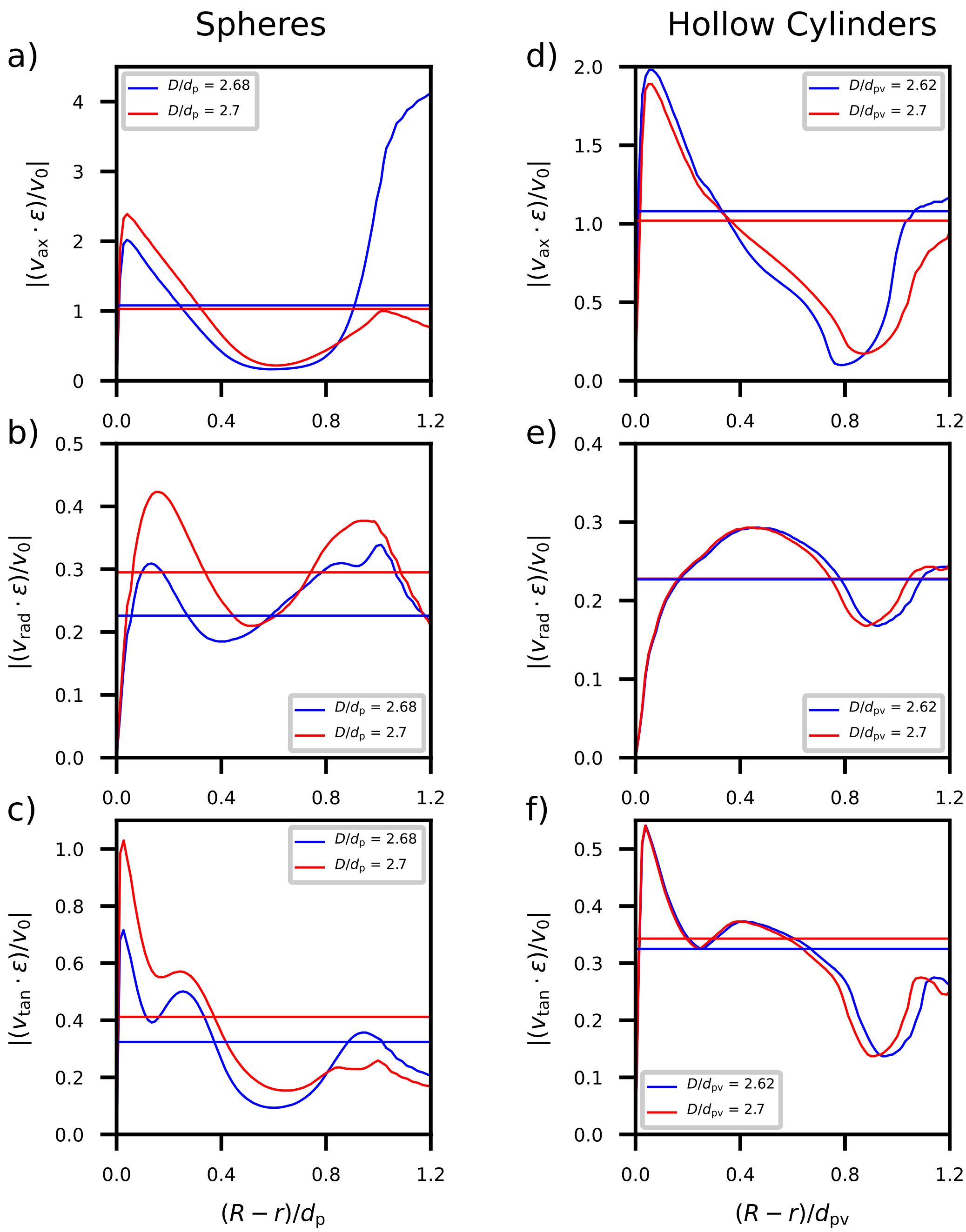

Figure 9: Normalized axial (top), radial (middle) and tangential (bottom) velocities in radial distance from the wall for spheres with *Central Channel* ($D/d_p = 2.68$) and without channel ($D/d_p = 2.7$) effect (a) - c)) and hollow cylinders (d) - f)) ($D/d_{pv} = 2.50$ and $D/d_{pv} = 2.62$)

Fig.9 d) shows the axial velocity components for two beds of hollow cylinders. The mean velocity value of the bed with $D/d_{\mathrm{pv}} = 2.62$ bed is slightly higher, resulting from a plateau with higher velocity from $(R-r)/d_{\mathrm{pv}} > 1$. This is due the more pronounced free space, as already seen in Fig. 3 b). This higher velocity shows a lower flow resistance in the axial direction of the bed. The radial velocity (Fig.9 e)) for both beds is similar. The difference in axial velocity results from the lower tangential velocity that the $D/d_{\mathrm{pv}} = 2.62$ bed has in comparison to the $D/d_{\mathrm{pv}} = 2.50$ bed (Fig.9 f)). The comparison of the radial velocity, and thus the radial mixing performance of the fixed bed, between the spheres in Fig. 9 b) and hollow cylinders in Fig. 9 e) shows that the mean value for spheres is still higher when the *Central Channel* is closed. This indicates a higher radial mixing for fixed beds of spheres, if no local structure effects occur.

3.5. Residence Time Distribution

3.5.1. Fixed Beds of Spheres

While the packed bed of spheres with $D/d_{\mathrm{p}} = 2.68$ forms a *Central Channel*, this channel is closed with a small change of D/d_{p} to 2.7. The resulting pressure drop can be predicted by the Eisfeld-Schnitzlein equation for the fixed bed without a channel, while it is overestimated for the other bed. The residence time sum curve (F curve) and the exit age distribution (E curve) are plotted in Fig. 10 a) and b), respectively, against the dimensionless residence time θ.

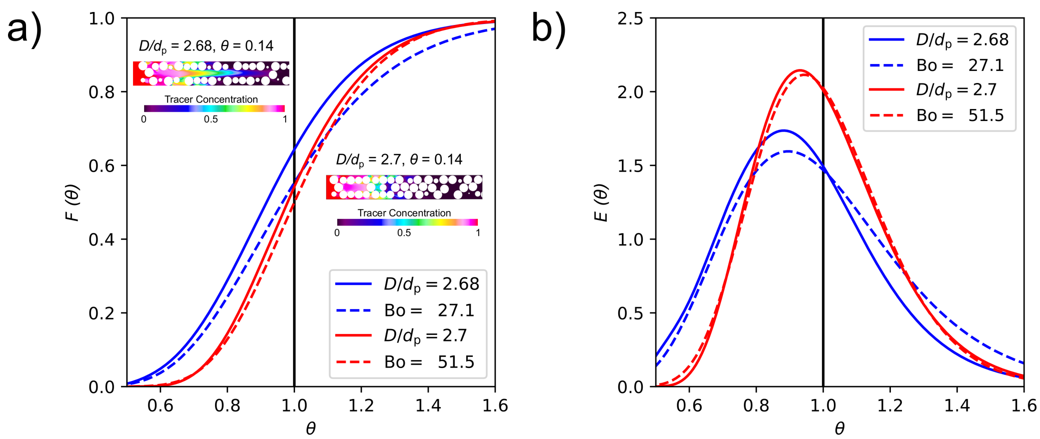

Figure 10: a) Residence time sum curve ($F = f(\theta)$ curve) and the exit age distribution ($E = f(\theta)$ curve) for fixed beds of spheres with $D/d_{\mathrm{p}} = 2.68$ and $D/d_{\mathrm{p}} = 2.7$ with consideration of convection only.

It can be seen that the fluid in the fixed bed with the *Central Channel* (blue solid line) leaves the reactor earlier than without a channel (red solid line). While for $D/d_{\mathrm{p}} = 2.68$ already 60 % leave the reactor at the hydrodynamic residence time $\theta = 1$, it is more symmetrical for the bed with $D/d_{\mathrm{p}} = 2.7$. Furthermore, it can be recognized that the reactor without a *Central Channel* can be described by a Bodenstein number of $\mathrm{Bo} = 51.5$ (red dotted line), while the fitted Bo for the fixed bed with a *Central Channel* is significantly lower ($Bo = 27.1$) (blue dotted line) and does not well describe the actual F curve. This is a result of the early curve behavior, which indicates stagnant zones in the fixed bed. This can be attributed to the fact that if the real vessel has no stagnant zones, the observed mean residence time $\bar{t}_{\mathrm{Obs}}$ has to be equal to the hydrodynamic mean residence time $\bar{t}_{\mathrm{Hy}}$ [49]. The active reactor volume V_{Active} can be quantified by comparing $\bar{t}_{\mathrm{Hy}}$ (Eq. (34)) with the $\bar{t}_{\mathrm{Obs}}$ (Eq. (35)) determined by the E and F curves.

$$\bar{t}_{\mathrm{Hy}} = \frac{V_{\mathrm{R}}}{\dot{V}} \tag{34}$$

$$\bar{t}_{\mathrm{Obs}} = \frac{V_{\mathrm{Active}}}{\dot{V}} \tag{35}$$

The hydrodynamic mean residence time $\bar{t}_{\mathrm{Hy}}$ can be calculated using the volumetric flow rate $\dot{V}$ and the reactor volume V_{R} available for the flow. On the other hand, the active reactor volume V_{Active} can be calculated using the observed mean residence time $\bar{t}_{\mathrm{Obs}}$ with the help of Eq (36).

$$V_{\mathrm{Active}} = \bar{t}_{\mathrm{Obs}} \cdot \dot{V} = \bar{t}_{\mathrm{Obs}} \cdot \frac{V_{\mathrm{R}}}{\bar{t}_{\mathrm{Hy}}} \tag{36}$$

With this connection, it follows that the percentage of the stagnant region can be determined by a comparison of the dimensionless residence times.

$$\frac{\overline{V}_{\mathrm{Active}}}{\overline{V}_{\mathrm{R}}} = \frac{\bar{\theta}_{\mathrm{Obs}}}{\bar{\theta}_{\mathrm{Hy}}} \tag{37}$$

The comparison shows, that for the $D/d_{\mathrm{p}} = 2.68$ fixed bed, a volume of 4.85 % is stagnant fluid. While it was possible to calculate the volume of stagnant fluid for the fixed bed configuration with $D/d_{\mathrm{p}} = 2.68$ at this point, as the mean residence times θ_{Hy} and θ_{Obs} differed, this was not possible for the other investigated fixed beds. In these cases, the observed mean residence times closely matched the hydrodynamic ones, indicating that no significant stagnant fluid volumes occur.

Fig. 11 shows the comparison between the beds of $D/d_\mathrm{p} = 2$ and $D/d_\mathrm{p} = 3.02$. Both fixed beds can be approximated with a corresponding Bo number. Again, there is a strong difference in RTD behavior between the two beds. While the fixed bed with $D/d_\mathrm{p} = 2.0$ shows a small $\mathrm{Bo} = 32.2$ number and thus a larger deviation from plug flow behavior, the fixed bed with $D/d_\mathrm{p} = 3.02$ shows an RTD curve that can be assumed as plug flow, since $\mathrm{Bo} > 100$. However, the fixed bed with $D/d_\mathrm{p} = 2.0$ does not show stagnant zones because the mean residence time $\overline{\theta}$ and the mean hydrodynamic residence time $\overline{\theta}_\mathrm{Hy}$ coincide.

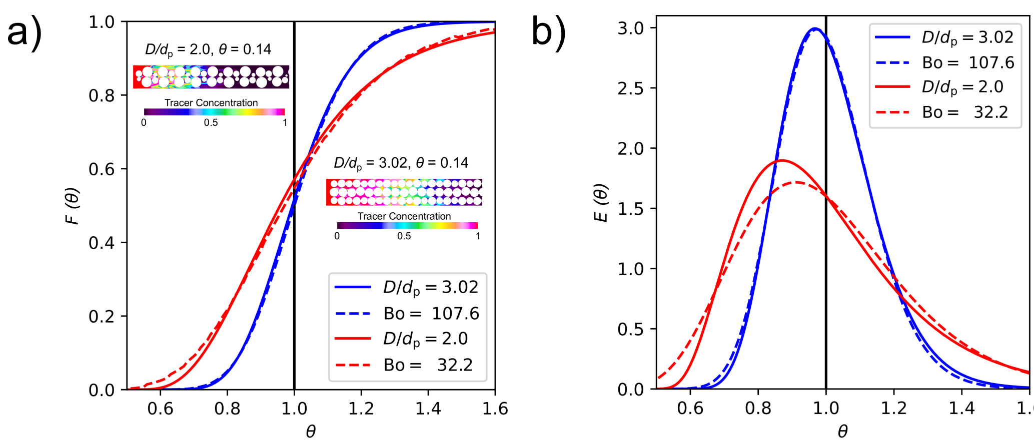

Figure 11: Residence time distribution sum (a)) and age distribution curve (b)) for fixed beds of spheres with $D/d_\mathrm{p} = 2$ and $D/d_\mathrm{p} = 3.02$ with consideration of convection only.

The reason for the plug flow behavior of the $D/d_\mathrm{p} = 3.02$ fixed bed, can be found in Fig. 12, where the seeds (streamlines of the flow simulation) for three different radial sections are shown at different axial coordinates. It can be observed that the seeds starting at an axial coordinate of $z = 0 = L/d_\mathrm{p} = 0$ already begin to mix after one particle diameter ($L/d_\mathrm{p} = 1$). The grey streamlines are displaced from the middle radial section towards the outer and central regions. After five particle diameters ($L/d_\mathrm{p} = 5$), red and green seeds are well mixed, which increases again after ten particle diameters ($L/d_\mathrm{p} = 10$).

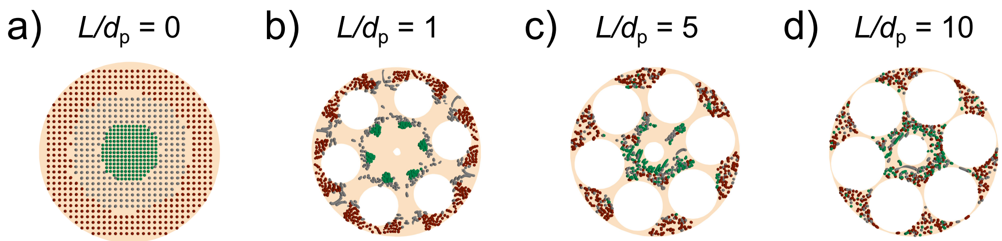

Figure 12: Seeds for visualization of the mixing properties of the fixed bed at a) axial coordinate $z = 0$, b) after one particle diameter, c) after 5 particle diameters, and d) after 10 particle diameters.

The following figure shows the comparison between a fixed bed with $D/d_{\mathrm{p}} = 3.2$ (red line), which has a partially blocked *Annular Gap*, and a fixed bed with $D/d_{\mathrm{p}} = 4.0$ (blue line), in which the two combined effects *Channel + Annular Gap* are present. It can be observed that the fixed bed with an *Annular Gap* can be can be described with a fitted Bodenstein number, similar to the fixed bed with $D/d_{\mathrm{p}} = 3.02$.

The Bodenstein number with a values of $\mathrm{Bo} = 78.0$ is lower than for a unblocked *Annular Gap*, but still indicates, that the reactor has an behavior close to plug flow.

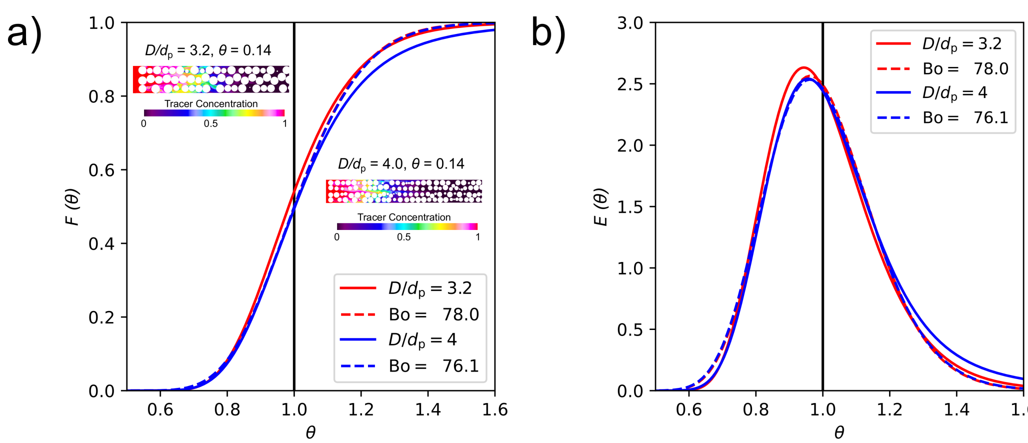

Figure 13: Residence time sum curve (F curve) and the exit age distribution (E curve) for fixed beds of spheres with $D/d_{\mathrm{p}} = 3.2$ and $D/d_{\mathrm{p}} = 4.0$ with consideration of convection only.

For the fixed bed with both structural effects, the fitted Bodenstein number is also high with a value of $\mathrm{Bo} = 76.1$ indicating also a plug flow-like behavior. Nevertheless, it can be seen, that the curve cannot fully represent the simulation results. This behavior is in accordance to the observations in Fig. 10, where also the *Central Channel* could not be reproduced. As the *Central Channel* effect is less pronounced in the $D/d_{\mathrm{p}} = 4.0$ fixed bed, it shows a higher accordance to the equation of Ogata and Banks [47].

3.5.2. Fixed Beds of Hollow Cylinders

Regarding the fixed beds composed of ring particles, it can be observed that although a Bodenstein number could be fitted for both D/d_{pv} values, it only partially corresponds to the simulated results. In both cases, the height and exact position of the maxima of the E-curve are not accurately matched. It is worth noting that both fixed beds exhibit a fairly similar Bodenstein number of 51.9 and 45.6. Nevertheless, the residence time behavior of the $D/d_{\mathrm{pv}} = 2.68$ bed shows an earlier maximum, resulting in an early curve behavior that can account for the observed pressure drop differences between correlation and experiment presented in Fig. 8.

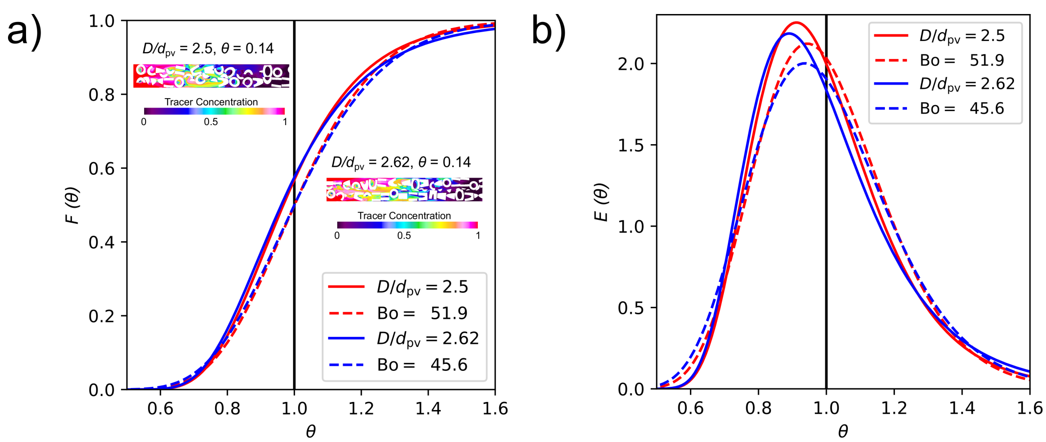

Figure 14: Residence time sum curve (F curve) and the exit age distribution (E curve) for fixed beds of rings with $D/d_{\mathrm{pv}} = 2.5$ and $D/d_{\mathrm{pv}} = 2.62$ with consideration of convection only.

4. Conclusion

The void fraction of packed beds, whether consisting of spherical particles or hollow cylinders, is difficult to predict due to the same scattering effects that can occur in both types of beds. Even small changes in the D/d_{pv} ratio can lead to significant changes in the structure and therefore in the overall void fraction. The structure effects of fixed beds consisting of monosized spheres can be classified into four categories: (i) *Single Particle String*, (ii) *Central Channel*, (iii) *Annular Gap*, and (iv) *Central Channel + Annular Gap*. These effects play a major role in the convective transport in fixed beds and thus highly affect the local and hence overall reactor behavior. The tortuosity of a fixed bed is introduced as another factor that can be helpful in describing the structure and the corresponding flow conditions. Therefore, pre-factors in the tortuosity formulation $\tau = a \cdot \varepsilon^{-1/3}$ have been proposed for slender packed beds with random structure and with *Central Channel* and *Annular Gaps*. However, when structure effects play a major role, pressure drop and Residence Time Distribution cannot be predicted reliably by the use of typical correlations. A significant discovery in this study is the linkage between the effects of the underlying structural elements and new factors in the Ergun equation. This development leads to a more accurate correlation compared to the original factors. The *Central Channel* has the greatest influence on pressure drop, which decreases with the opening of the channel until it is partially blocked, after which it immediately increases again. This makes the fixed bed random again, and the pressure drop can also be predicted correctly by original correlations. The *Annular Gap* has a smaller but more constant influence on pressure drop, while the *Central Channel + Annular Gap* has an influence between the two single effects.

The RTD shows significant differences between beds. The *Central Channel* has the lowest pressure drop but also the lowest value of the corresponding Bodenstein number, indicating non-ideal behavior in terms of lateral mixing. Furthermore, the residence time distribution analysis revealed that the central channel contributes to the occurrence of stagnant volumes. Consequently, approximately 4.85 % of the fluid volume experiences stagnation, which, in conjunction with the central channel, leads to an extreme fronting of the residence time. The *Annular Gap* is associated with the highest Bodenstein number and a smaller pressure drop than randomized beds, with the highest Bodenstein number being idealized as plug flow behavior and found for $D/d_\mathrm{p} = 3.02$. The fixed beds with an *Annular Gap* seems to be a reactor configuration that combines desirable effects, as it provides plug flow behavior and a reduced pressure drop. Furthermore, as already indicated in our previous works, in the range of $D/d_\mathrm{p} = 3.02$, the fixed bed forms a structure with a repeating pattern. This is reflected in the narrow distribution of void fraction with $\bar{\varepsilon} = 0.412$ and a low standard deviation $\sigma = 0.0014$. This indicates that the behavior of a fixed bed in the range of $D/d_\mathrm{p} = 3$ can be well predicted, as the same structure forms with high regularity.

For fixed beds of hollow cylinders, it has been observed that even a small change in the D/d_{pv} ratio can lead to large deviations of the correlations used to predict pressure drop. In contrast to fixed beds composed of monodisperse spheres, the underlying effects in hollow cylinder beds have proven to be less straightforward to identify. Instead of a continuous channel, partial small channel pathways are formed through stacking of the hollow cylinders (clusters of stacked pellets), which reduce flow resistance. Furthermore, the analysis of velocity fields has revealed that the investigated rings do not offer intensified radial mixing compared to beds made of spheres. In the residence time distribution, it was also observed that despite their different pressure drop characteristics, which could be described by correlations in one case ($D/d_{\mathrm{pv}} = 2.5$) and not in the other ($D/d_{\mathrm{p}} = 2.68$), both fixed beds exhibited similar behavior and thus similar Bodenstein numbers. The fitted Bodenstein number for these beds was in the same range ($\mathrm{Bo} = 51.9$ and $\mathrm{Bo} = 45.6$) as that of the randomly structured spherical fixed bed with $D/d_{\mathrm{p}} = 2.7$ ($\mathrm{Bo} = 51.9$).

In conclusion, this study has demonstrated the occurrence of different structures in fixed beds and their influence on pressure drop, tortuosity, velocity field, and residence time behavior. Categorizing these effects across the D/d_{p} range allows for predictions of their occurrence and their associated impacts, while the modified factors for tortuosity and pressure drop correlations enable predictive modeling.

5. Acknowledgments

This publication is based upon work supported and financed by Clausthal University of Technology, project Catalytic and microbial methanation as basis for sustainable energy storage (CliMb). The authors would like to thank Jule Kersebaum for her great support in carrying out the experimental work for this publication.

Symbols used

Latin Letters

a		form factor
A		viscous term of the Ergun equation (*Blake-Kozeny-Carman* constant)
A	m^2	cross sectional area of reactor tube
A_w		wall correction term of Eisfeld-Schnitzlein equation
B		inertial term of the Ergun equation (*Burke-Plummer* constant)
$B\mathrm{w}$		wall correction term of Eisfeld-Schnitzlein equation
Bo		Bodenstein number
C_m	$\mathrm{kg\,m^{-2}\,s^{-1}}$	weight flow rate
d	m	diameter
D	m	reactor diameter
D_ax	$\mathrm{m^2\,s^{-1}}$	axial dispersion coefficient
$\mathbf{D}$	$\mathrm{s^{-1}}$	deformation tensor
E		RTD density function
f_p		friction factor
F		RTD sum function
h	m	height
$\mathbf{I}$		unit tensor
k	$\mathrm{W\,m^{-1}\,K^{-1}}$	heat conductivity
L	m	fixed bed length
m		internal volume flow rate
N		particle count
p	Pa	pressure
$\dot{Q}$	W	heat flux
r	m	radial coordinate
R	m	reactor radius
Re_p^*		modified particle Reynolds number
S	m^2	surface
t	s	time
$\bar{t}$	s	mean residence time
T	K	temperature
$\mathbf{T}$	Pa	stress tensor
v	$\mathrm{m\,s^{-1}}$	velocity
$\mathbf{v}$	$\mathrm{m\,s^{-1}}$	velocity vector
V	m^3	volume
$\dot{V}$	$\mathrm{m^3\,s^{-1}}$	volume flow rate

Greek Letters

Δ		difference
ε		mean void fraction
θ		dimensionless residence time
$\bar{\theta}$		dimensionless mean residence time
μ	$\mathrm{kg\,m^{-1}\,s^{-1}}$	dynamic viscosity
ρ	$\mathrm{kg\,m^{-3}}$	fluid density
τ		tortuosity
Φ		passive scalar component

Sub- and superscripts

0	superficial
active	refers to the active reactor volume through which flow occurs
ax	axial
Bed	fixed bed
CV	control volume
eq	equivalent
free	refers to the free Volume
full	refers to the full Volume
fc	full cylinder
hc	hollow cylinder
Hy	hydrodynamic
i	inner
o	outer
Obs	observed
p	particle
particles	refers to the cumulative volume of all particles
pv	volume equivalent
R	reactor
rad	radial
Rel	relative
tan	tangential

Abbreviations

CFD	computational fluid dynamics
PRCFD	particle-resolved computational fluid dynamics
RANS	Reynolds averaged Navier Stokes
RBA	rigid body approach
RTD	residence time distribution
SIMPLE	semi-implicit method for pressure linked equations

References

[1] G. Eigenberger, W. Ruppel, Catalytic Fixed-Bed Reactors, in: Wiley-VCH Verlag GmbH & Co. KGaA (Ed.), Ullmann's Encyclopedia of In-

dustrial Chemistry, Wiley-VCH Verlag GmbH & Co. KGaA, Weinheim, Germany, 2012, pp. 1–60. doi:10.1002/14356007.b04_199.pub2.

[2] A. G. Dixon, Heat transfer in fixed beds at very low (< 4) tube-to-particle diameter ratio, Industrial & Engineering Chemistry Research 36 (8) (1997) 3053–3064. doi:10.1021/ie9605950.

[3] K. Ridgway, K. J. Tarbuck, Radial voidage variation in randomly-packed beds of spheres of different sizes, Journal of Pharmacy and Pharmacology 18 (Supplement_1) (1966) 168S–175S. doi:10.1111/j.2042-7158.1966.tb07980.x.

[4] G. E. Mueller, Radial void fraction distributions in randomly packed fixed beds of uniformly sized spheres in cylindrical containers, Powder Technology 72 (3) (1992) 269–275. doi:10.1016/0032-5910(92)80045-X.

[5] M. Giese, K. Rottschäfer, D. Vortmeyer, Measured and modeled superficial flow profiles in packed beds with liquid flow, AIChE Journal 44 (2) (1998) 484–490. doi:10.1002/aic.690440225.

[6] S. Flaischlen, G. D. Wehinger, Synthetic packed-bed generation for CFD simulations: Blender vs. STAR-CCM+, ChemEngineering 3 (2) (2019) 52. doi:10.3390/chemengineering3020052.

[7] S. Flaischlen, S. Lipp, B. Kreitz, J. Martin, T. Turek, G. D. Wehinger, Particle–resolved CFD simulations for diluted catalytic fixed–bed reactors: Methanation of CO_2, Chemie Ingenieur Technik 92 (9) (2020) 1349–1350. doi:10.1002/cite.202055357.

[8] S. Flaischlen, M. Kutscherauer, G. D. Wehinger, Local structure effects on pressure drop in slender fixed beds of spheres, Chemie Ingenieur Technik 93 (1-2) (2021) 273–281. doi:10.1002/cite.202000171.

[9] Z. Guo, Z. Sun, N. Zhang, M. Ding, J. Wen, Experimental characterization of pressure drop in slender packed bed ($1 < D/d < 3$), Chemical Engineering Science 173 (2017) 578–587. doi:10.1016/j.ces.2017.08.022.

[10] A. G. Dixon, Local structure effects on heat transfer in very low tube-to-particle diameter ratio fixed beds of spheres, Industrial & Engineering Chemistry Research 60 (27) (2021) 9777–9786. doi:10.1021/acs.iecr.1c01660.

[11] J. von Seckendorff, K. Achterhold, F. Pfeiffer, R. Fischer, O. Hinrichsen, Experimental and numerical analysis of void structure in random packed beds of spheres, Powder Technology 380 (2021) 613–628. doi:10.1016/j.powtec.2020.11.026.

[12] G. F. Froment, Analysis and design of fixed bed catalytic reactors, in: J. L. Margrave (Ed.), Mass Spectrometry in Inorganic Chemistry, Vol. 109 of Advances in Chemistry, American Chemical Society, Washington, D.C., 1968, pp. 1–55. doi:10.1021/ba-1972-0109.ch001.

[13] B. D. Kulkarni, L. K. Doraiswamy, Estimation of effective transport properties in packed bed reactors, Catalysis Reviews 22 (3) (1980) 431–483. doi:10.1080/03602458008067540.

[14] S. Ergun, Fluid flow through packed columns, Chemical Engineering Progress 48 (1952) 89–94.

[15] B. Eisfeld, K. Schnitzlein, The influence of confining walls on the pressure drop in packed beds, Chemical Engineering Science 56 (14) (2001) 4321–4329. doi:10.1016/S0009-2509(00)00533-9.

[16] A. G. Dixon, General correlation for pressure drop through randomly-packed beds of spheres with negligible wall effects, AIChE Journal 69 (6) (2023) e18035. doi:10.1002/aic.18035.

[17] N. Jurtz, P. Waldherr, M. Kraume, Numerical analysis of the impact of particle friction on bed voidage in fixed–beds, Chemie Ingenieur Technik 66 (5) (2019) 705. doi:10.1002/cite.201800190.

[18] A. G. Dixon, B. Partopour, Computational Fluid Dynamics for Fixed Bed Reactor Design, Annual Review of Chemical and Biomolecular Engineering 11 (1) (2020) 109–130. doi:10.1146/annurev-chembioeng-092319-075328.

[19] N. Jurtz, G. D. Wehinger, U. Srivastava, T. Henkel, M. Kraume, Validation of pressure drop prediction and bed generation of fixed-beds with complex particle shapes using discrete element method and computational fluid dynamics, AIChE Journal 66 (6) (2020) e16967. doi:10.1002/aic.16967.

[20] N. Jurtz, S. Flaischlen, S. C. Scherf, M. Kraume, G. D. Wehinger, Enhancing the thermal performance of slender packed beds through internal heat fins, Processes 8 (12) (2020) 1528. doi:10.3390/pr8121528.

[21] G. D. Wehinger, M. Kraume, CFD als Designtool für Festbettreaktoren mit kleinem Rohr-zu-Pelletdurchmesser-Verhältnis: Heute oder in Zukunft?, Chemie Ingenieur Technik 89 (4) (2017) 447–453. doi:10.1002/cite.201600155.

[22] T. Eppinger, K. Seidler, M. Kraume, DEM-CFD simulations of fixed bed reactors with small tube to particle diameter ratios, Chemical Engineering Journal 166 (1) (2011) 324–331. doi:10.1016/j.cej.2010.10.053.

[23] G. D. Wehinger, C. Fütterer, M. Kraume, Contact modifications for CFD simulations of fixed-bed reactors: Cylindrical particles, Industrial & Engineering Chemistry Research 56 (1) (2017) 87–99. doi:10.1021/acs.iecr.6b03596.

[24] M. Kutscherauer, S. Böcklein, G. Mestl, T. Turek, G. D. Wehinger, An improved contact modification routine for a computationally efficient cfd simulation of packed beds, Chemical Engineering Journal Advances 9 (2022) 100197. doi:10.1016/j.ceja.2021.100197.

[25] G. D. Wehinger, T. Eppinger, M. Kraume, Detailed numerical simulations of catalytic fixed-bed reactors: Heterogeneous dry reforming of methane, Chemical Engineering Science 122 (2015) 197–209. doi:10.1016/j.ces.2014.09.007.

[26] N. Jurtz, G. D. Wehinger, U. Srivastava, T. Henkel, M. Kraume, Validation of pressure drop prediction and bed generation of fixed-beds with complex particle shapes using discrete element method and computational fluid dynamics, AIChE Journal 66 (6) (2020) e16967. doi:10.1002/aic.16967.

[27] G. D. Wehinger, B. Kreitz, A. Nagy, T. Turek, Characterization of a modular Temkin reactor with experiments and computational fluid dynamics simulations, Chemical Engineering Journal 389 (2020) 124342. doi:10.1016/j.cej.2020.124342.

[28] G. D. Wehinger, Particle-resolved CFD simulations of catalytic flow reactors (2016). doi:10.14279/depositonce-5432.

[29] G. R. George, M. Bockelmann, L. Schmalhorst, D. Beton, A. Gerstle, A. Lindermeir, G. D. Wehinger, Radial heat transport in a fixed-bed reactor made of metallic foam pellets: Experiment and particle-resolved computational fluid dynamics, International Journal of Heat and Mass Transfer 197 (2022) 123376. doi:https://doi.org/10.1016/j.ijheatmasstransfer.2022.123376.

[30] G. D. Wehinger, F. Klippel, M. Kraume, Modeling pore processes for particle-resolved CFD simulations of catalytic fixed-bed reactors, Computers & Chemical Engineering 101 (2017) 11–22. doi:10.1016/j.compchemeng.2017.02.029.

[31] P. T. Vallano, V. T. Remcho, Assessment of electroosmotic perfusion in capillary chromatographic columns using electrical conductivity, The Journal of Physical Chemistry B 105 (16) (2001) 3223–3228. doi:10.1021/jp003525m.

[32] S. J. Cooper, D. S. Eastwood, J. Gelb, G. Damblanc, D. Brett, R. S. Bradley, P. J. Withers, P. D. Lee, A. J. Marquis, N. P. Brandon, P. R. Shearing, Image based modelling of microstructural heterogeneity in lifepo 4 electrodes for Li-ion batteries, Journal of Power Sources 247 (2014) 1033–1039. doi:10.1016/j.jpowsour.2013.04.156.

[33] D. Emmel, J. D. Hofmann, T. Arlt, I. Manke, G. D. Wehinger, D. Schröder, Understanding the impact of compression on the active area of carbon felt electrodes for redox flow batteries, ACS Applied Energy Materials 3 (5) (2020) 4384–4393. doi:10.1021/acsaem.0c00075.

[34] A. Bufe, G. Brenner, Systematic study of the pressure drop in confined geometries with the lattice boltzmann method, Transport in Porous Media 123 (2) (2018) 307–319. doi:10.1007/s11242-018-1043-0.

[35] J. von Seckendorff, N. Szesni, R. Fischer, O. Hinrichsen, Experimental characterization of random packed spheres, cylinders and rings, and their influence on pressure drop, Chemical Engineering Science 222 (2020) 115644. doi:10.1016/j.ces.2020.115644.

[36] R. Langsch, J. Zalucky, S. Haase, R. Lange, Investigation of a packed bed in a mini channel with a low channel-to-particle diameter ratio: Flow regimes and mass transfer in gas–liquid operation, Chemi-

cal Engineering and Processing: Process Intensification 75 (2014) 8–18. doi:10.1016/j.cep.2013.10.004.

[37] A. G. Dixon, Correlations for wall and particle shape effects on fixed bed bulk voidage, The Canadian Journal of Chemical Engineering 66 (5) (1988) 705–708. doi:10.1002/cjce.5450660501.

[38] L. Shen, Z. Chen, Critical review of the impact of tortuosity on diffusion, Chemical Engineering Science 62 (14) (2007) 3748–3755. doi:10.1016/j.ces.2007.03.041.

[39] D. A. G. Bruggeman, Berechnung verschiedener physikalischer Konstanten von heterogenen Substanzen. I. Dielektrizitätskonstanten und Leitfähigkeiten der Mischkörper aus isotropen Substanzen, Annalen der Physik 416 (7) (1935) 636–664. doi:10.1002/andp.19354160705.

[40] G. H. Neale, W. K. Nader, Prediction of transport processes within porous media: Diffusive flow processes within an homogeneous swarm of spherical particles, AIChE Journal 19 (1) (1973) 112–119. doi:10.1002/aic.690190116.

[41] K. A. Akanni, J. W. Evans, I. S. Abramson, Effective transport coefficients in heterogeneous media, Chemical Engineering Science 42 (8) (1987) 1945–1954. doi:10.1016/0009-2509(87)80141-0.

[42] R. J. Millington, Gas diffusion in porous media, Science 130 (3367) (1959) 100–102. doi:10.1126/science.130.3367.100.a.

[43] J. van Brakel, P. M. Heertjes, Analysis of diffusion in macroporous media in terms of a porosity, a tortuosity and a constrictivity factor, International Journal of Heat and Mass Transfer 17 (9) (1974) 1093–1103. doi:10.1016/0017-9310(74)90190-2.

[44] J. C. Maxwell, A Treatise on Electricity and Magnetism: pt. III. Magnetism. pt. IV. Electromagnetism, Clarendon Press, 1881.

[45] D. Nemec, J. Levec, Flow through packed bed reactors: 1. single-phase flow, Chemical Engineering Science 60 (24) (2005) 6947–6957. doi:10.1016/j.ces.2005.05.068.

[46] G. Sonntag, Einfluß des Lückenvolumens auf den Druckverlust in gasdurchströmten Füllkörpersäulen, Chemie Ingenieur Technik 32 (5) (1960) 317–329. doi:10.1002/cite.330320502.

[47] A. Ogata, R. B. Banks, A solution of the differential equation of longitudinal dispersion in porous media (1961). doi:10.3133/pp411A.

[48] A. de Klerk, Voidage variation in packed beds at small column to particle diameter ratio, AIChE Journal 49 (8) (2003) 2022–2029. doi:10.1002/aic.690490812.

[49] O. Levenspiel, Chemical Reaction Engineering, 3rd Edition, Wiley, New York, 1999.